

# Partial-aperture array imaging in acoustic waveguides

Chrysoula Tsogka<sup>1</sup>, Dimitrios A. Mitsoudis<sup>2</sup>, Symeon Papadimitropoulos<sup>3</sup>

<sup>1</sup> Department of Mathematics and Applied Mathematics, University of Crete & IACM/FORTH, Heraklion 70013, Greece. (tsogka@tem.uoc.gr)

<sup>2</sup> Department of Energy Technology Engineering, Technological Educational Institute of Athens & IACM/FORTH, Heraklion 70013, Greece. (dmits@teiath.gr)

<sup>3</sup> Department of Mathematics and Applied Mathematics, University of Crete & IACM/FORTH, Heraklion 70013, Greece. (spapadem@tem.uoc.gr)

**Abstract.** We consider the problem of imaging extended reflectors in waveguides using partial array aperture, *i.e.*, an array that does not span the whole depth of the waveguide. To image we employ a method that back-propagates a weighted modal projection of the usual array response matrix. The challenge in this setup is to correctly define this projection matrix in order to maintain some nice energy concentration properties for the imaging method that were obtained previously in [36] for the full aperture case. We propose in this paper a way for achieving this and study the properties of the resulting imaging method.

*Keywords:* array imaging, waveguides, partial aperture, prolates

## 1. Introduction

We consider the problem of detecting and imaging *extended* impenetrable obstacles in a finite in depth and infinite in range two-dimensional acoustic waveguide. Sound pulses are generated by a vertical array of transducers with *partial aperture*, *i.e.*, an array that does not span the whole depth of the waveguide. The term *extended* is used to indicate that the typical size of the reflectors is comparable to the acoustic wavelength. The current work is based, and extends to the partial-aperture array case, the methodology that we have proposed in [36], where we have studied the problem of imaging extended scatterers in waveguides selectively using a vertical full-aperture array of transducers. We have in mind applications in underwater acoustics where sound waves are used to probe the sea and their echoes are recorded and analysed in order to detect submerged objects. The marine environment that we consider is modelled as an infinite strip of constant depth. Although this is a simplified and rather ideal model of a marine acoustic environment it still carries and exhibits the main features and challenges of acoustic wave propagation in the sea.

We now present the main features of the imaging problem that we are interested in. We assume that an array consisting of  $N$  transducers is set vertically in the waveguide. At first, each element of the array acts as a point source and emits a sound pulse, whose echoes are recorded in all the elements of the array that now act as receivers. In this way it is formed an  $N \times N$  matrix  $\widehat{\Pi}$ ; this is the so-called *array response matrix*. Specifically, we shall consider that we are given the array response matrix for the scattered field, where this is obtained, as usually, by subtracting the incident field from the total field. Given these data, we want to create images of parts of the waveguide that would assist us to decide whether a scatterer is present or not. The usual procedure in imaging is summarised in the following steps: a) We determine a bounded subdomain of the waveguide that is usually called the *search domain*, b) we discretize the search domain, and c) in each node of the search domain we associate the value of an imaging functional. Then the graph of this functional forms the image that we are looking for, where, usually, peaks that are related with the functional's maxima indicate the presence of the scatterer. Examples of widely used imaging techniques include the *Kirchhoff Migration functional* (KM) (see [4, §9]), the *matched field functional* (see [18]), the linear sampling [8, 9, 21] and the factorization method [2].

The problem of detecting obstacles in waveguides has been studied extensively using various techniques in several configurations related to applications such as marine acoustics, inspection of underground pipes, etc. Indicatively, for mathematical investigation of inverse scattering problems in homogeneous acoustic waveguides with horizontal or planar boundaries we refer to [16, 11, 26], see also [10] and the references therein. Of course, to image accurately an extended reflector one should take full advantage of information that emanates from its edges. This is the concept of selective imaging for extended reflectors that was inspired from the concept of selective focusing, and the associated well-known DORT method, [24, 27], which allows one to derive images

that focus selectively on each one of several point (or small) scatterers in a medium. In [6], the so-called subspace projection method was used to image selectively the edges of extended scatterers in free space. In the same spirit, in our earlier work, [36], we have proposed an alternative functional, that was based on Kirchhoff migration, and on a weighted modal projection of the array response matrix denoted by  $\widehat{\mathbb{P}}$ , to selectively image extended scatterers in waveguides using an active array of sensors which spans the whole depth of the waveguide.

In this paper we briefly review our imaging approach and consider a simplified model problem where the scatterer is a vertical one-dimensional perfect reflector; from now on will be referred to as screen. The object is twofold: First, we pursue the analysis of the spectral properties of the weighted modal projection of the array response matrix,  $\widehat{\mathbb{P}}$ , and we investigate the relation between  $\widehat{\mathbb{P}}$  and its singular vectors, with the well known *prolate matrix* and the *prolate spheroidal wave functions*, respectively, which have been analyzed in a series of outstanding papers by Slepian, Pollak and Landau, [34, 19, 20, 31, 32]. Second, the screen model problem and the properties of the singular vectors of  $\widehat{\mathbb{P}}$  are used in order to appropriately modify our approach to handle the case of a partial-aperture array. This is of practical importance in applications since often the arrays that are used do not span the whole depth of the waveguide, see, *e.g.*, [15] for a shallow-water experiment conducted in the Mediterranean Sea. However, the extension from full- to partial-aperture array case is not at all straightforward since key properties, like the orthonormality of the vertical eigenfunctions along the array, do not hold any more. We therefore propose an appropriate definition of the weighted projected matrix  $\widehat{\mathbb{P}}$  for the partial aperture case and study the performance of the corresponding imaging functional for the screen model problem as we decrease the array aperture.

The paper is organised as follows. In Section 2 we formulate the imaging problem and briefly review our selective imaging approach. In Section 3 we study the screen model problem in the full-aperture case and establish the relation with the prolate spheroidal wave functions. In Section 4 we appropriately modify our approach to handle the case of a partial-aperture array. In Section 5 we present the outcome of some numerical simulations that we have performed for more general extended scatterers such as a square and a disc. Moreover, we test our methodology in a waveguide with depth-dependent sound speed profile.

## 2. Formulation of the problem

In this work, we study the problem of imaging extended reflectors in an infinite, homogeneous two-dimensional acoustic waveguide with horizontal boundaries, using an array  $\mathcal{A}$  that consists of  $N$  transducers that can act both as sources and receivers. The term ‘extended’ indicates that the size of the scatterer is comparable to the acoustic wavelength. The array is set vertically in the waveguide and may or may not span the whole depth of the waveguide; we refer to the latter case as *partial aperture* imaging. Specifically, our infinite waveguide is  $\mathbb{R} \times [0, D]$  in Cartesian coordinates  $(z, x)$ , where

the horizontal  $z$ -axis denotes the range and the vertical  $x$ -axis the depth (assumed to be positive downward). A single scatterer, denoted by  $\mathcal{O}$ , is located in the waveguide, see Figure 1. Then the total acoustic pressure field  $p^{\text{tot}}$  satisfies the wave equation

$$\Delta p^{\text{tot}}(t, \vec{x}) - \frac{1}{c_0^2} \frac{\partial^2 p^{\text{tot}}(t, \vec{x})}{\partial t^2} = -f(t, \vec{x}), \quad (1)$$

where the source term models a point-like source with time harmonic dependence. A Dirichlet (pressure release) condition is imposed on the two horizontal boundaries, and we assume a suitable radiation condition, and that  $p^{\text{tot}}(t, \vec{x}) = 0$  for  $t \leq 0$ . Moreover, the scatterer  $\mathcal{O}$  is considered to be acoustically hard, hence a homogeneous Neumann condition is imposed on  $\partial\mathcal{O}$ . Taking the Fourier transform

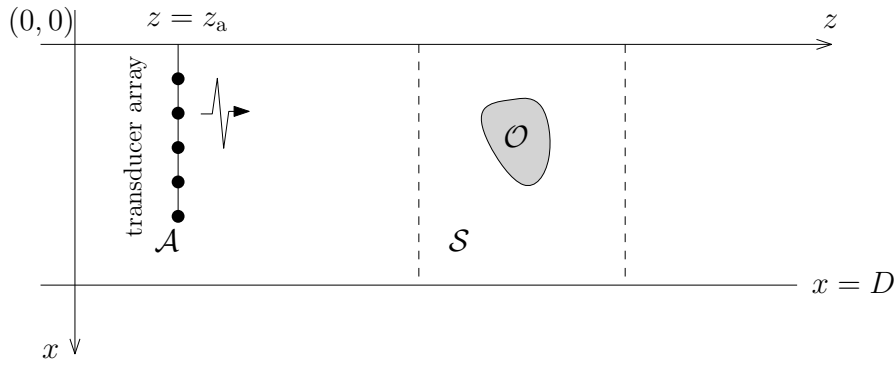


Figure 1: Schematic depiction of the waveguide imaging problem.

$$\widehat{p}^{\text{tot}}(\omega, \vec{x}) = \int e^{i\omega t} p^{\text{tot}}(t, \vec{x}) dt,$$

we obtain from (1) the Helmholtz equation

$$-\Delta \widehat{p}^{\text{tot}}(\omega, \vec{x}) - k^2 \widehat{p}^{\text{tot}}(\omega, \vec{x}) = \widehat{f}(\omega, \vec{x}), \quad (2)$$

where  $k = \omega/c_0$  is the real wavenumber,  $\omega$  is the angular frequency, and  $\lambda = 2\pi/k$  is the wavelength.

In what follows we shall also need the outgoing Green's function  $\widehat{G}(\vec{x}, \vec{x}_s)$  of the Helmholtz operator due to a point source located at  $\vec{x}_s = (z_s, x_s)$ , where  $\vec{x} = (z, x) \in \mathbb{R} \times (0, D)$ . Here  $\widehat{G}$  is expressed in terms of its usual normal mode representation, [17, 26],

$$\widehat{G}(\vec{x}, \vec{x}_s) = \frac{i}{2} \sum_{n=1}^{\infty} \frac{1}{\beta_n} e^{i\beta_n |z-z_s|} X_n(x) X_n(x_s), \quad (3)$$

where  $\{\mu_n, X_n\}_{n=1,2,\dots}$  are the eigenvalues and corresponding orthonormal eigenfunctions of the two-point vertical eigenvalue problem

$$X''(x) + \mu X(x) = 0, \quad x \in (0, D) \quad \text{and} \quad X(0) = X(D) = 0,$$

and are given by

$$\mu_n = (n\pi/D)^2, \quad X_n(x) = \sqrt{2/D} \sin(\sqrt{\mu_n} x), \quad n = 1, 2, \dots \quad (4)$$

Moreover, the  $\beta_n$  are the horizontal wavenumbers, defined as

$$\beta_n = \begin{cases} \sqrt{k^2 - \mu_n}, & 1 \leq n \leq M, \\ i\sqrt{\mu_n - k^2}, & n \geq M + 1. \end{cases} \quad (5)$$

where we have assumed that for each frequency there exists an index  $M$  such that

$$\mu_M < k^2 < \mu_{M+1}.$$

The first  $M$  eigenvalues correspond to the *propagating* modes, while the rest to the *evanescent* modes that decay exponentially with range.

### 2.1. Array imaging setup

We assume that the data that we have in our disposal are tabulated in the so-called *array response matrix*, henceforth denoted as  $\widehat{\Pi}$ ; an  $N \times N$  complex matrix whose  $(r, s)$  element is the Fourier transform of the echoes recorded on the  $r$ -th transducer (acting as a receiver) due to a  $\delta$ -function impulse generated by the  $s$ -th transducer (acting as a source), for a given frequency  $\omega$ . Specifically, we shall consider that we are given the array response matrix for the scattered field formulated, as usual, by subtracting the incident field from the total field. We also assume that the transducers are distributed uniformly on the array, and that the array is quite dense, *i.e.* the inter-element array distance  $h$  is appropriately small.

In this work we are mainly going to make use of an imaging functional, denoted by  $\widetilde{\mathcal{I}}^{\text{KM}}$ , that was introduced in [36] and is defined as

$$\widetilde{\mathcal{I}}^{\text{KM}}(\vec{\mathbf{y}}^s, \omega) = -\frac{1}{4h^2} \sum_{m,n=1}^M e^{-i(\beta_m + \beta_n)|z_a - z^s|} X_n(x^s) X_m(x^s) \widehat{\mathbb{P}}_{mn}(\omega), \quad (6)$$

for a single frequency  $\omega$ , where  $\vec{\mathbf{y}}^s = (z^s, x^s)$  denotes a point in our search domain  $\mathcal{S}$  and  $z_a$  is the location in range of our array. The  $M \times M$  matrix  $\widehat{\mathbb{P}}$  is a weighted modal projection of the array response matrix, and in the full array case ( $\mathcal{A} = [0, D]$ ) is given by the relation

$$\widehat{\mathbb{P}}_{mn}(\omega) = \beta_m \beta_n \int_{\mathcal{A}} dx_s \int_{\mathcal{A}} dx_r \widehat{\Pi}(\vec{\mathbf{x}}_s, \vec{\mathbf{x}}_r, \omega) X_m(x_s) X_n(x_r), \quad m, n = 1, \dots, M. \quad (7)$$

We use for our functional the symbol  $\widetilde{\mathcal{I}}^{\text{KM}}$  to distinguish it from the classical *Kirchhoff migration (KM)* functional, [5, 7],

$$\mathcal{I}^{\text{KM}}(\vec{\mathbf{y}}^s, \omega) = \sum_{r=1}^N \overline{\widehat{G}(\vec{\mathbf{x}}_r, \vec{\mathbf{y}}^s, \omega)} \sum_{s=1}^N \widehat{\Pi}(\vec{\mathbf{x}}_r, \vec{\mathbf{x}}_s, \omega) \overline{\widehat{G}(\vec{\mathbf{x}}_s, \vec{\mathbf{y}}^s, \omega)}, \quad (8)$$

where  $\widehat{G}$  is the Green's function defined in (3), and the bars denote complex conjugation.

Furthermore, we may reconstruct specific parts of the scatterer by means of a selective imaging technique, called the subspace projection method [6], which is based

on the singular value decomposition (SVD) of the matrix  $\widehat{\mathbb{P}}(\omega)$ . To be more specific, let us write the SVD of  $\widehat{\mathbb{P}}(\omega)$  in the form:

$$\widehat{\mathbb{P}}(\omega) = \sum_{i=1}^{\rho} \sigma_i \mathcal{U}_i \mathcal{V}_i^*,$$

where  $\sigma_1 \geq \dots \geq \sigma_{\rho} > \sigma_{\rho+1} = \dots = \sigma_M = 0$  are the singular values,  $\rho = \text{rank}(\widehat{\mathbb{P}}(\omega))$ , and  $\mathcal{U}_i, \mathcal{V}_i$  are the left and right singular vectors, respectively.

This allows us to create a filtered version of the matrix  $\widehat{\mathbb{P}}(\omega)$  as

$$D[\widehat{\mathbb{P}}(\omega)] = \sum_{i=1}^{\rho} d_i \sigma_i \mathcal{U}_i \mathcal{V}_i^*,$$

where the  $d_i$ 's may be viewed as filter weights. In our case,  $d_i = 1$  or  $0$ , depending whether we take the  $i$ -th singular vector into account in the computation of the filtered version of the matrix, or not. Based on this filtered version of the matrix  $\widehat{\mathbb{P}}$ , we define the functionals

$$\widetilde{\mathcal{I}}^{\text{KM},f}(\vec{\mathbf{y}}^s, \omega) = -\frac{1}{4h^2} \sum_{m,n=1}^M e^{-i(\beta_n + \beta_m)|z_a - z^s|} X_n(x^s) X_m(x^s) \left( D[\widehat{\mathbb{P}}(\omega)] \right)_{mn}, \quad (9)$$

and

$$\widetilde{\mathcal{I}}_J^{\text{KM}}(\vec{\mathbf{y}}^s, \omega) = -\frac{1}{4h^2} \sum_{m,n=1}^M e^{-i(\beta_n + \beta_m)|z_a - z^s|} X_n(x^s) X_m(x^s) \left( \sigma_J(\omega) \mathcal{U}_J(\omega) \mathcal{V}_J^*(\omega) \right)_{mn}, \quad (10)$$

where  $\widetilde{\mathcal{I}}_J^{\text{KM}}$  corresponds to the case where we project just on the  $J$ -th singular vector, *i.e.*  $d_J = 1$  and  $d_i = 0$  for all  $i \neq J$ .

### 3. A model problem: Connection with band-limited functions

In this section we revisit a simplified model problem that we have introduced in [36]. There are two main reasons for that: First, we provide some new results that allow us to clarify further the performance of  $\widetilde{\mathcal{I}}^{\text{KM}}$  in this ideal setting, and, second, this model problem will serve as a guide in order to extend the applicability of our imaging approach in the case of the partial array; this will be pursued in the next section.

Now we briefly present the model problem and summarize some known results that will be useful to us in what follows. In the waveguide described in the previous section we assume that the array passes through the  $x$  axis, and that  $N$  transducers that span the whole depth of the waveguide are located equidistantly at depths  $x_i = ih$ ,  $1 \leq i \leq N$ , where  $h := D/(N+1)$ . The scatterer  $\mathcal{T}$  is a one-dimensional vertical mirror, a ‘screen’, located at range  $z = L$ , see Figure 2. Let the coordinates of its endpoints be  $(L, \alpha)$  and  $(L, \beta)$ , hence its width equals  $b = \beta - \alpha$ , and let us denote by  $\mathcal{C}$  the vertical section of the waveguide at range  $z = L$ , *i.e.*,  $\mathcal{C} := \{(L, x) : 0 \leq x \leq D\}$ .

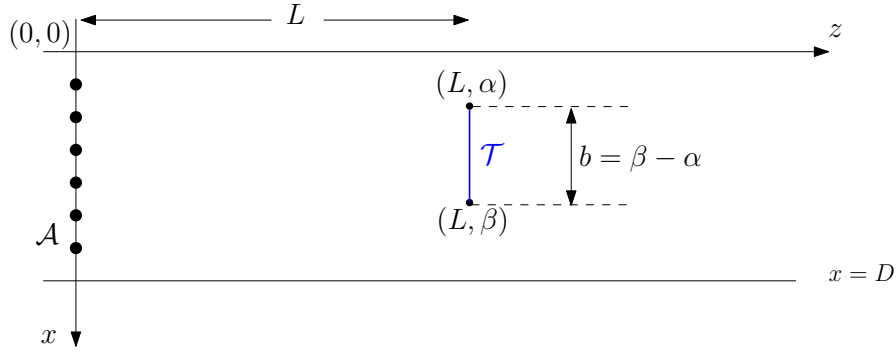


Figure 2: Sketch of a one-dimensional vertical scatterer ('screen')  $\mathcal{T}$  and basic notation.

We assume that each point of the target has unit reflectivity, thus the Born approximation allows us to ideally express the  $(r, s)$ -entry of the array response matrix as

$$\widehat{\Pi}(\vec{\mathbf{x}}_r, \vec{\mathbf{x}}_s, \omega) = k^2 \int_{\mathcal{T}} \widehat{G}(\vec{\mathbf{y}}, \vec{\mathbf{x}}_r) \widehat{G}(\vec{\mathbf{y}}, \vec{\mathbf{x}}_s) dx, \quad (11)$$

where the source is now located at  $\vec{\mathbf{x}}_s = (0, x_s)$ , the receiver at  $\vec{\mathbf{x}}_r = (0, x_r)$ ,  $s, r \in \{1, 2, \dots, N\}$ ,  $\vec{\mathbf{y}} = (L, x)$ ,  $x \in [\alpha, \beta]$ , and  $\widehat{G}$  is the Green's function defined in (3). Recall that  $\mu_n$ ,  $X_n$  are the eigenvalues and corresponding orthonormal eigenfunctions of the operator  $-d^2/dx^2$  in  $H^2(0, D) \cap H_0^1(0, D)$ , defined in (4), and  $\beta_n$  are the horizontal wavenumbers defined in (5).

In the following we suppress the multiplicative constant  $k^2$ , we insert (3) into (11) and take into account that when  $L$  is sufficiently large the terms  $(e^{-\sqrt{\mu_m - k^2}L})/\sqrt{\mu_m - k^2}$ , for  $m \geq M + 1$ , are practically zero. These allow us to approximate the array response matrix as

$$\widehat{\Pi}(\vec{\mathbf{x}}_r; \vec{\mathbf{x}}_s, \omega) = -\frac{1}{4} \sum_{m,n=1}^M \frac{e^{i\beta_m L}}{\beta_m} X_m(x_s) X_n(x_r) \frac{e^{i\beta_n L}}{\beta_n} \int_{\beta}^{\alpha} X_m(x) X_n(x) dx, \quad (12)$$

or, equivalently, as a matrix product of the form

$$\widehat{\Pi} = -\frac{1}{4} V D_{\beta} Q A_M Q D_{\beta} V^T, \quad (13)$$

where

$$D_{\beta} = \text{diag}(1/\beta_1, \dots, 1/\beta_M), \quad Q = \text{diag}(e^{i\beta_1 L}, \dots, e^{i\beta_M L}), \quad (14)$$

$V$  is the  $N \times M$  matrix with

$$V_{k\ell} = X_{\ell}(x_k), \quad k = 1, \dots, N, \ell = 1, \dots, M, \quad (15)$$

and  $A_M$  is the matrix with entries

$$a_{mn} = \int_{\alpha}^{\beta} X_m(x) X_n(x) dx, \quad m, n = 1, 2, \dots, M. \quad (16)$$

Now, the orthonormality of the eigenfunctions  $\{X_n\}_{n=1,2,\dots}$  implies that the matrix  $\widehat{\mathbb{P}}$  that is defined in (7), and is employed in the definition (6) of the functional  $\widetilde{\mathcal{I}}^{\text{KM}}$ , is related to the matrix  $A_M$  as follows

$$\widehat{\mathbb{P}} = -\frac{1}{4}QA_MQ, \quad (17)$$

where  $Q$  is the diagonal matrix  $\text{diag}(e^{i\beta_1L}, \dots, e^{i\beta_ML})$ . Hence, up to a multiplicative constant,  $\widehat{\mathbb{P}}$  is unitarily equivalent to  $A_M$ .

Therefore, the spectral properties of  $A_M$  play an important role in understanding the behavior of the imaging functional  $\widetilde{\mathcal{I}}^{\text{KM}}$ . One may easily check that  $A_M$  is a real, symmetric *Toeplitz-minus-Hankel* matrix, with its generating function being the indicator function of  $\mathcal{T}$ , [36]. Specifically,

$$A_M = T_M - H_M, \quad \text{where } T_M := (t_{\ell-m})_{\ell,m=1}^M, \quad H_M := (t_{\ell+m})_{\ell,m=1}^M,$$

and

$$t_m = \frac{1}{D} \int_0^D \mathbb{1}_{\mathcal{T}}(x) \cos \frac{m\pi x}{D} dx, \quad (18)$$

where  $\mathbb{1}_{\mathcal{T}}(x)$  is the indicator function of  $\mathcal{T}$ .

Now, let us introduce some notation that is fairly standard, see *e.g.* [35, 1]: Let  $\mathbb{J}$  be the flip matrix (i.e. the matrix that has ones on the secondary diagonal and zeros elsewhere). Then, a vector  $\mathbf{x} \in \mathbb{R}^n$  is called symmetric if  $\mathbb{J}\mathbf{x} = \mathbf{x}$  and skew-symmetric if  $\mathbb{J}\mathbf{x} = -\mathbf{x}$ . Moreover, an eigenvalue  $\nu$  of a matrix  $T$  is defined to be even (odd) if  $T$  has a symmetric (skew-symmetric)  $\nu$ -eigenvector.

Classical results by Szegő, [13, pp. 64-65], and Trench, [35], allow us to characterize fully the eigenvalues of  $A_M$ ; for details we refer to [36]. Specifically, the eigenvalues of  $A_M$  are the odd eigenvalues of the  $(2M+1) \times (2M+1)$  Toeplitz matrix  $T_{2M+1}$ , and they are clustered emphatically near 0 and 1. To be precise, if  $\mathbf{u} = (u^1, \dots, u^M)^T$  is an orthonormal eigenvector of  $A_M$  that corresponds to an eigenvalue  $\nu$ , then

$$\mathbf{v} = 2^{-1/2} \begin{pmatrix} -\mathbb{J}\mathbf{u} \\ 0 \\ \mathbf{u} \end{pmatrix} = 2^{-1/2} (-u_M, \dots, -u_1, 0, u_1, \dots, u_M)^T \quad (19)$$

is an orthonormal skew-symmetric  $\nu$ -eigenvector of  $T_{2M+1}$ , and vice versa. We shall say that eigenvectors that correspond to eigenvalues that are close to 1 comprise the signal subspace, those that correspond to eigenvalues that are close to 0 comprise the noise subspace, and, finally, the eigenvectors that correspond to intermediate eigenvalues form the transient subspace. Moreover, we may estimate the number of ‘significant’ singular values for the matrix  $A_M$ : It is approximately equal to

$$\left\lceil M \frac{b}{D} \right\rceil \approx \left\lceil \frac{2b}{\lambda} \right\rceil. \quad (20)$$

where  $\lambda$  is the wavelength,  $M = \lfloor \frac{2D}{\lambda} \rfloor$  is the number of propagating modes in the waveguide, and  $b$  is the width of the screen. Recalling that the cross-range resolution is  $\lambda/2$ , we conclude that the rank of the matrix  $A_M$  is roughly equal to the size of the

object divided by the ‘array resolution’. This result was already known to hold in the free-space case (see [6, §4.5.2]).

Next, we consider the imaging functional  $\tilde{\mathcal{I}}_J^{\text{KM}}$  evaluated at a search point  $\vec{\mathbf{y}}^s = (L, x^s)$  that is located at the correct range  $L$ . Note that the subscript  $J$  indicates that for selective imaging only the  $J$ -th singular vector is employed in the approximation of the matrix  $\widehat{\mathbb{P}}$ . Then, from (10) and (17) we have that

$$\tilde{\mathcal{I}}_J^{\text{KM}}(\vec{\mathbf{y}}^s) = \sigma_J \left( \frac{1}{4h} \sum_{n=1}^M u_n^J X_n(x^s) \right)^2 = (8Dh^2)^{-1} \sigma_J \left( \sum_{n=1}^M u_n^J \sin \frac{n\pi x^s}{D} \right)^2, \quad (21)$$

where  $\mathbf{u}^J = (u_1^J, u_2^J, \dots, u_M^J)^T$  is the singular vector of  $A_M$  that corresponds to the singular value  $\sigma_J$ . Hence, the  $\tilde{\mathcal{I}}_J^{\text{KM}}$  functional at the correct range is in fact, up to a constant, the square of the trigonometric polynomial

$$p_J(x) = (2/D)^{1/2} \sum_{n=1}^M u_n^J \sin \frac{n\pi x}{D}. \quad (22)$$

The orthonormality of the vertical eigenfunctions and a one line calculation imply that

$$\frac{\|p_J\|_{L^2[\alpha, \beta]}^2}{\|p_J\|_{L^2[0, D]}^2} = \frac{\int_{\alpha}^{\beta} p_J^2(x) dx}{\int_0^D p_J^2(x) dx} = \frac{\sum_{n,m=1}^M (A_M)_{mn} u_n^J u_m^J}{\sum_{m=1}^M (u_m^J)^2} = \sigma_J.$$

Therefore the trigonometric polynomial that corresponds to the first singular vector  $\mathbf{u}^1$  and, consequently, the associated image computed at the correct range  $L$ , exhibit the largest fractional concentration of energy in  $(\alpha, \beta)$ .

Now we are in a position to scrutinize the form of the singular vectors of the matrix  $A_M$ . In [36] we have derived some analytic expressions for those singular vectors which correspond to singular values that are close to 1. In the remaining part of the section we provide explicit characterizations for the singular vectors of  $A_M$  depending on the various positions of the screen.

### 3.1. A screen attached on the top of the waveguide

Assume that the screen is attached on the top of the waveguide, *i.e.*  $\mathcal{T} = \{(L, x) : x \in [0, b]\}$ . In this case the eigenvectors of the matrix  $A_M$  may be recovered through (19) by the skew-symmetric eigenvectors of the matrix  $T_{2M+1}$  which satisfy

$$\sum_{n=-M}^M \frac{1}{(m-n)\pi} \sin \frac{(m-n)\pi b}{D} u_n^J = \nu_J u_m^J, \quad m = -M, \dots, M,$$

where skew-symmetry implies that  $u_{-i}^J = -u_i^J$ ,  $i = 1, \dots, M$ . Therefore, in this case  $\{u_i^J\}_{i=-M}^M$  may be identified as a skew-symmetric *discrete prolate spheroidal sequence (DPSS)*, [32], (also known as a *Slepian sequence*) which is a discrete analog of the *prolate spheroidal wave function (PSWF)*  $\psi_{2J-1}$ , [34]. Specifically,  $\psi_n$  is the eigenfunction that corresponds to the  $n$ -th eigenvalue of the Fredholm integral equation

$$\int_{-1}^1 \frac{\sin c(x-y)}{\pi(x-y)} \psi_n(y) dy = \nu_n \psi_n(x), \quad x \in [-1, 1], \quad (23)$$

where, in our case, the so-called bandwidth parameter is  $c = 2\pi b/\lambda = bk$ ,  $k$  being the wavenumber. The PSWFs possess many interesting properties, see *e.g.* [34, 33, 23]. Here we just name two: The eigenvalues are discrete and form a decreasing sequence  $\nu_0 > \nu_1 > \dots$  that tends to zero as  $n \rightarrow \infty$ , and the corresponding eigenfunctions  $\psi_n(x)$  are even or odd with  $n$ .

Now, letting  $y_n = \frac{\lambda n}{2D}$  ( $\lambda$  is the wavelength), we may interpret the trigonometric polynomial  $p_J$  in (22) as a Riemann sum that approximates the integral

$$\begin{aligned} \frac{2\sqrt{2D}}{\lambda} \int_0^1 \psi_{2J-1}(y) \sin(\xi y) dy &= \frac{\sqrt{2D}}{i\lambda} \int_{-1}^1 \psi_{2J-1}(y) e^{i\xi y} dy \\ &= \gamma_{2J-1} \psi_{2J-1}\left(\frac{x}{b}\right), \quad x \in [0, D], \end{aligned}$$

where  $\xi := 2\pi x/\lambda = kx$ , and the first equality holds since  $\psi_{2J-1}$  is an odd function in  $[-1, 1]$ , while the second equality reflects the interesting property that the Fourier transform of a PSWF restricted to  $[-1, 1]$  is invariant except for a horizontal stretching, [33, Eq. (24)]; note that  $\gamma_{2J-1}$  is independent of  $x$ .

In order to illustrate these conclusions we consider a waveguide with depth equal to  $D = 200$  m and constant sound speed equal to  $c_0 = 1500$  m/s. The frequency is equal to 73 Hz, hence the wavelength  $\lambda \approx 20.548$  m, and the screen's width equals  $b = 40$  m. Then,  $M = 19$  modes propagate in the waveguide and according to (20) we expect  $A_M$  to possess four 'significant' singular values. Indeed, the first three lie close to 1, the fourth is approximately 0.62, the fifth one is approximately equal to 0.04, while the rest are less than  $4 \times 10^{-4}$  and decrease rapidly to zero. In Figure 3 we superimpose the graph of the trigonometric polynomial  $(p_J(x))^2$  on the graph of the PSWF  $\left(\psi_{2J-1}\left(\frac{x}{b}\right)\right)^2$ , both normalised with respect to their maximum values, for  $x \in [0, D]$ , and for  $J = 1, 2, \dots, 6$ .

As expected, these functions for  $J = 1$  to 4 are mainly supported in  $[0, b] = [0, 40]$ , while for  $J = 5$  and 6 they are supported in the exterior of  $[0, b]$ .

### 3.2. A screen attached on the bottom of the waveguide

In this case let  $\mathcal{T} = \{(L, x) : x \in [D - b, D]\}$ . Then it is easy to check that the entries of the matrix  $A_M$  satisfy

$$a_{mn} = \int_{D-b}^D X_m(x) X_n(x) dx = (-1)^{m+n} \int_0^b X_m(x) X_n(x) dx,$$

and, consequently, if  $\mathbf{u} = (u_i)_{i=1}^M$  is a  $\nu$ -eigenvector of  $A_M$  when the screen is attached on the top of the waveguide, then one may show that  $\mathbf{v} := (v_i)_{i=1}^M = ((-1)^{i+1} u_i)_{i=1}^M$  is a  $\nu$ -eigenvector of  $A_M$  when the screen is attached on the bottom of the waveguide. Moreover, let us denote, for the moment,  $p_J^{\text{top}}(x) = \sum_{n=1}^M u_n^J X_n(x)$  to be the trigonometric polynomial for a screen attached on the top of the waveguide, and  $p_J^{\text{bot}}(x) = \sum_{n=1}^M v_n^J X_n(x)$  to be the corresponding trigonometric polynomial for a screen attached on the bottom of the waveguide. Then it is easy to show that

$$p_J^{\text{bot}}(x) = p_J^{\text{top}}(D - x),$$

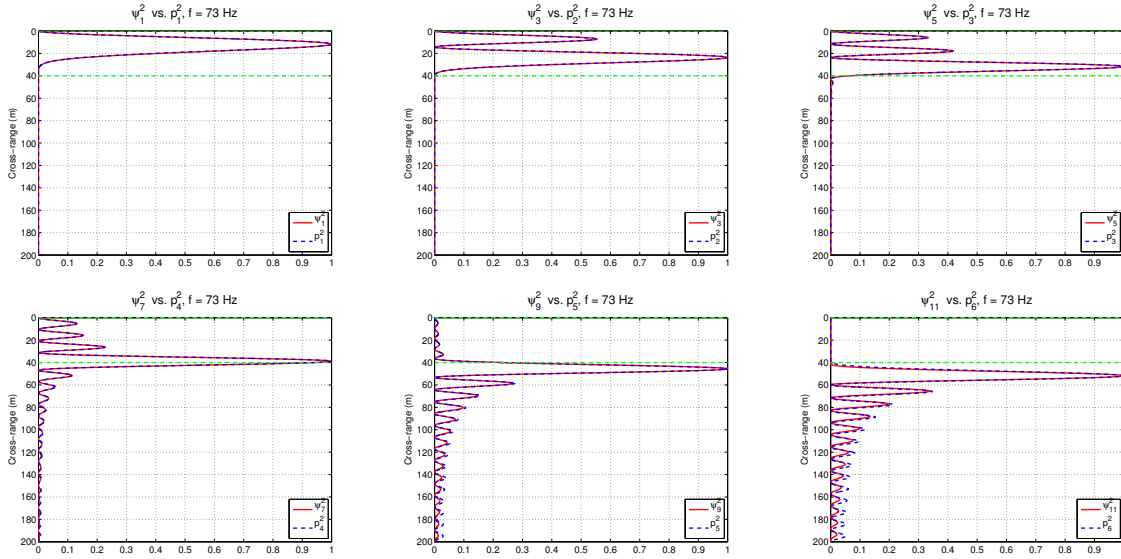


Figure 3: The graph of  $(p_J(x))^2$  (dashed line printed in blue) superimposed on the graph of  $(\psi_{2J-1}(\frac{x}{b}))^2$  (solid line printed in red), for  $x \in [0, 200]$ . (Both are normalised with respect to their maximum values.) Top row:  $J = 1, 2, 3$ , bottom row:  $J = 4, 5, 6$ . The frequency is  $f = 73$  Hz, and the width of the screen  $b = 40$  m.

which implies that the image created by the imaging functional  $\tilde{\mathcal{I}}_J^{KM}$ , at the correct range  $L$ , is determined by the graph of the PSWF  $(\psi_{2J-1}(\frac{D-x}{b}))^2$ ,  $x \in [0, D]$ .

### 3.3. A screen located in the interior of the waveguide

In this case let  $\mathcal{T} = \{(L, x) : x \in [\alpha, \beta] \subset [0, D]\}$ . Eq. (19) suggests, as before, that the eigenvectors of  $A_M$  are determined through the skew-symmetric eigenvectors of the matrix  $T_{2M+1}$ , where they now satisfy the system of equations

$$\sum_{n=-M}^M \frac{1}{(m-n)\pi} \left( \sin \frac{(m-n)\pi\beta}{D} - \sin \frac{(m-n)\pi\alpha}{D} \right) u_n^J = \nu_J u_m^J, \quad (24)$$

for  $m = -M, \dots, M$ . Equations (24) may be viewed as the discrete analog of the following integral equation

$$K_1 u(x) := \int_{-1}^1 \frac{1}{\pi(x-y)} \left( \sin \frac{2\pi\beta}{\lambda}(x-y) - \sin \frac{2\pi\alpha}{\lambda}(x-y) \right) u(y) dy = \nu u(x), \quad (25)$$

for  $x \in [-1, 1]$ , where we have suppressed the index  $J$  for notational convenience. Note that the kernel in (25) is more complicated than the sinc kernel appearing in (23) that concerns the limiting case where the screen is attached on the top of the waveguide. Eq. (25) has been studied in [29] where the authors consider a time–frequency concentration problem for signals that have a prescribed bandwidth of the form  $|w| \in [a, b]$  for  $0 < a < b$ ; thus the frequency interval is not connected any longer. Moreover, for general values of  $\alpha$  and  $\beta$  ( $\alpha < \beta$ ) the work of Morrison [25], and SenGupta

et al. [29], indicates that there cannot be found a second or fourth-order self-adjoint linear differential operator with polynomial coefficients that commutes with the integral operator  $K_1$  defined in (25). The fact that in the case of Section 3.1 the corresponding integral operator commutes with a quite simple second-order differential operator is crucial for the analysis conducted by Slepian and his colleagues at Bell Laboratories, [34, 19, 20, 31, 32].

Therefore we are not able to characterise completely the eigenfunctions of (25), as was the case with the the eigenfunctions of (23) that were identified as PSWF's. Nevertheless, the integral operator  $K_1$  is a compact symmetric operator from  $L^2[-1, 1]$  to  $L^2[-1, 1]$ , hence its eigenvalues  $\nu_0 \geq \nu_1 \geq \dots \geq \nu_n \geq \dots \rightarrow 0$ , as  $n \rightarrow \infty$ , while its corresponding eigenfunctions are complete in  $L^2[-1, 1]$ , [29].

Working as in Section 3.1 we may view the trigonometric polynomial  $p_J(x) = (2/D)^{1/2} \sum_{n=1}^M u_n^J \sin \frac{n\pi x}{D}$  as an approximation of the integral

$$\frac{\sqrt{2D}}{\lambda} i \int_{-1}^1 e^{i\xi y} u(y) dy, \quad \xi = 2\pi x/\lambda = kx,$$

where  $u$  is an *odd* eigenfunction of the integral equation (25) that corresponds to the eigenvalue  $\sigma_J$ . Interestingly enough, one may follow the lines of SenGupta et al. in [29], in order to prove that

$$\int_{-1}^1 e^{i\xi y} u(y) dy = Cv(x), \quad x \in [0, D],$$

where  $v$  is a  $\sigma_J$ -eigenfunction of the integral equation

$$K_2 v(x) := \int_{\mathcal{J}} \frac{\sin k(x-y)}{\pi(x-y)} v(y) dy = \nu v(x), \quad (26)$$

for  $x \in \mathcal{J} := [-\beta, -\alpha] \cup [\alpha, \beta]$ . Here we stress the fact that in (26),  $\mathcal{J}$  is the disconnected interval  $[-\beta, -\alpha] \cup [\alpha, \beta]$ , while the kernel is a sinc function with bandwidth parameter equal to the wavenumber. Note that  $K_2$  is also a compact symmetric operator from  $L^2(\mathcal{J})$  to  $L^2(\mathcal{J})$ , that has the same eigenvalues with (25), and its corresponding eigenfunctions are complete in  $L^2(\mathcal{J})$ , [29].

Hence, the output of the imaging functional  $\tilde{\mathcal{I}}_J^{\text{KM}}$  when it is evaluated at the correct range (see (21)) is recovered by the graph of the eigenfunction of (26) that corresponds to the eigenvalue  $\sigma_J$ . Note that the domain of the eigenfunctions  $v$  is extended for values of  $x$  outside  $\mathcal{J}$ , as usual, by using the left hand side of (26), that is well defined for  $x \in \mathcal{J}$ , in order to define  $v$  for values of  $x$  that lie outside  $\mathcal{J}$ . Specifically, let

$$v(x) = \frac{1}{\nu} \int_{\mathcal{J}} \frac{\sin k(x-y)}{\pi(x-y)} v(y) dy, \quad x \notin \mathcal{J}.$$

These remarks are illustrated in Figure 4 where we plot superimposed the graph of  $p_J^2(x)$  and the graph of the square of the corresponding eigenfunction of (26), normalised with respect to their  $L_\infty$ -norms. All the physical parameters are the same as those used in

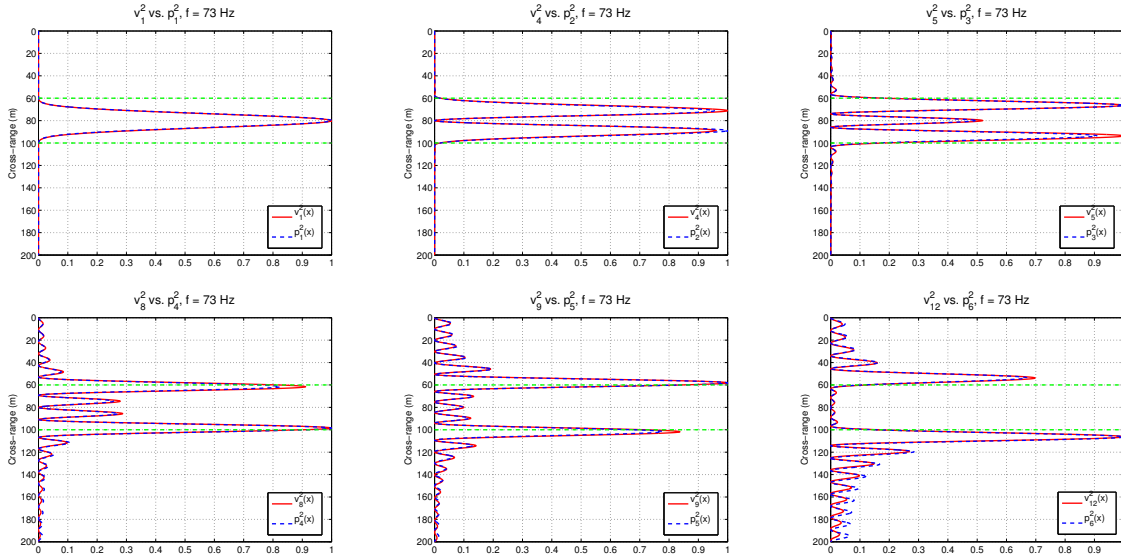


Figure 4: The graph of  $(p_J(x))^2$  (dashed line printed in blue) superimposed on the graph of the square of the corresponding eigenfunction of (26) (solid line printed in red), for  $x \in [0, 200]$ . (Both are normalised with respect to their maximum values.) The ordinates  $\alpha = 60$  and  $\beta = 100$  are printed in green dashed lines. Top row:  $J = 1, 2, 3$ , bottom row:  $J = 4, 5, 6$ . The frequency is  $f = 73$  Hz,  $D = 200$  m, and the width of the screen  $b = 40$  m.

Figure 3, while the ordinates of the screen's endpoints are  $\alpha = 60$  m,  $\beta = 100$  m, thus the width of the screen is again  $b = 40$  m.

As one may immediately verify there is very good agreement between the graphs of  $p_J^2(x)$  and the corresponding eigenfunctions of (26) squared. Moreover, notice that, for example,  $p_1^2(x)$  that corresponds to the largest eigenvalue (approximately equal to one) exhibits a peak around the midpoint of the screen,  $p_4^2(x)$  that corresponds to an eigenvalue  $\approx 0.640$  peaks near the endpoints of  $\mathcal{T}$ , while  $p_6^2(x)$  that corresponds to an eigenvalue  $\approx 0.025$  is practically supported in the exterior of  $\mathcal{T}$ .

**Remark 1** We close this section with a discussion concerning possible generalizations of the theory presented here:

- (i) The theory for the considered model problem can be generalized to the three dimensional case for a waveguide with a bounded rectangular cross-section. In this case, to allow for exploiting tensor product expressions the array should be planar and the equivalent of the one dimensional screen would be a two-dimensional rectangular planar screen. Both the array and the screen should be perpendicular to the horizontal direction which is assumed to be the direction of propagation.
- (ii) Considering a general reflector geometry is more challenging. Indeed, we can always write the matrix  $\hat{\mathbb{P}}$  in the form of (17). This means that  $\hat{\mathbb{P}}$  can be always decomposed as a product of a unitary propagator matrix  $Q$  that transfers the field from the array to the range of the reflector times the matrix  $A_M$  that carries information about the

reflector, times the same unitary matrix  $Q$  that now transfers the scattered field from the reflector to the array. Therefore, the matrix  $\widehat{\mathbb{P}}$  is unitarily equivalent to the matrix  $A_M$  and information about the reflector can be obtained from the singular value decomposition of  $\widehat{\mathbb{P}}$ . Although, the structure of the matrix  $A_M$  does not have in general the exact Hankel-minus-Toeplitz form observed for the screen model problem, we expect that the conclusions drawn from the model problem carry over to more general reflector's geometries. In particular, as our numerical results suggest, information about the reflector's location and shape can be obtained from the singular vectors that correspond to the largest and intermediate singular values with the first ones focusing to the bulk of the reflector and the second ones focusing to its boundary.

#### 4. Partial aperture

We have spent the previous section reviewing and analyzing the performance of the imaging functional  $\widetilde{\mathcal{I}}^{\text{KM}}$  in the screen model-problem under the assumption that the array spans the whole depth of the waveguide. Our main interest in this article, however, is in imaging extended reflectors with a *partial* array. In what follows, we therefore consider the screen model-problem with an array that does not span the whole  $[0, D]$ . Then the vertical eigenfunctions  $X_n$  are no longer orthonormal along the array, and one may immediately check that  $\widehat{\mathbb{P}}$  as defined in (7) is no more unitarily equivalent to  $A_M$ . This of course affects the efficiency of  $\widetilde{\mathcal{I}}^{\text{KM}}$  in selective imaging in the sense that we lose the usual ‘ordering’ of images which implies that projection of  $\widehat{\mathbb{P}}$  on its first singular vector exhibits focusing at the center of the reflector, while projecting on subsequent significant singular vectors results in images that focus at the endpoints of the reflector, [6, 36]. Even if we cast aside selectivity and concentrate in creating images with  $\widetilde{\mathcal{I}}^{\text{KM}}$  we will soon discover, as one would expect, that the efficiency of  $\widetilde{\mathcal{I}}^{\text{KM}}$  deteriorates as we decrease the length  $l_{\text{arr}}$  of the array. We illustrate this with the following example. We consider a sound speed  $c_0 = 1500$  m/s, the reference frequency is  $f_0 = 75$  Hz, hence the reference wavelength  $\lambda_0 = 20$  m, and the depth of the waveguide is taken equal to  $D = 200$  m. All the experiments shown here are performed for a single frequency  $f = 73$  Hz at which  $M = 19$  modes propagate. The scatterer, i.e. the screen, is centered at  $(L, x_0) = (410, 100)$  m and its length is  $b = 40$  m  $= 2\lambda_0$ . The inter-element array distance  $h = \lambda_0/8 = 2.5$  m, unless stated otherwise. In the leftmost subplot of Figure 5 we show the image we obtain with  $\widetilde{\mathcal{I}}^{\text{KM}}$  for full array, while the other three subplots from left to right are created with array length  $l_{\text{arr}} = 180, 140,$  and  $100$  m, respectively. In all cases the length of the array is reduced symmetrically from both ends. Moreover, to assess the noise level of an image, we define the Signal-to-Noise Ratio (SNR) by,

$$\text{SNR} = \frac{\max_{\vec{x}^s \in \mathcal{R}} |\widetilde{\mathcal{I}}^{\text{KM}}(\vec{x}^s)|}{\max_{\vec{x}^s \in \mathcal{S} \setminus \mathcal{R}} |\widetilde{\mathcal{I}}^{\text{KM}}(\vec{x}^s)|},$$

where  $\mathcal{R}$  is a subset of our search domain  $\mathcal{S}$  that contains the reflector. In our tests we define  $\mathcal{R}$  as a  $6\lambda_0 \times 6\lambda_0$  box with the scatterer lying at its center. The SNR value can be used as a quantitative measure that corroborates the qualitative characteristics of the image. In Figure 5, and in what follows, the boundary of  $\mathcal{R}$  is drawn in red. As it is evident from Figure 5, and the associated SNR values shown in the title of each subplot, the quality of the image deteriorates as  $l_{\text{arr}}$  decreases.

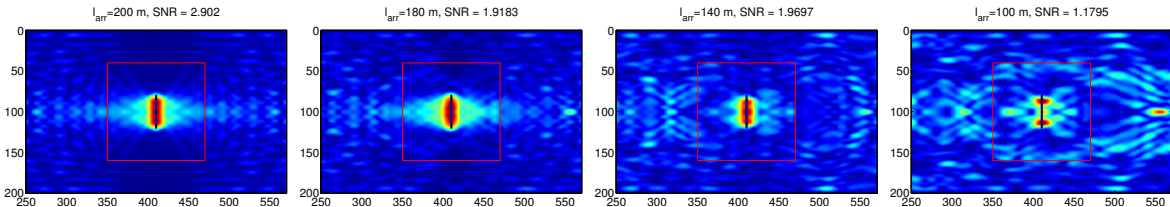


Figure 5: Imaging with  $\tilde{\mathcal{I}}^{\text{KM}}$  for the screen. The length of the array from left to right is  $l_{\text{arr}} = 200, 180, 140, 100$  m, respectively, the frequency equals  $f = 73$  Hz and the width of the screen  $b = 40$  m.

Let us remark here that this is not a limitation of the particular imaging functional and, in general, a deterioration of the imaging results is expected as the array aperture decreases. Similar results not shown here are also obtained with the classical  $\mathcal{I}^{\text{KM}}$  imaging functional. Next, we will propose an alternative definition of the matrix  $\hat{\mathbb{P}}$  in order to preserve the nice properties that we have observed in the full array case to the case of the partial-aperture array as well.

#### 4.1. Weighted projection of the array response matrix for the partial array case:

##### Motivation

Now, we shall present a way to construct a weighted projection of the array response matrix in the case of the partial-aperture array. Our observations in Section 3 regarding the band-limited nature of the trigonometric polynomials with coefficients the eigenvectors of the matrix  $A_M$  lead us to consider the  $M \times M$  matrix with entries

$$(A_{\text{arr}})_{mn} = \int_{\mathcal{A}} X_m(x)X_n(x)dx, \quad m, n = 1, \dots, M. \quad (27)$$

$A_{\text{arr}}$  is a real, symmetric Toeplitz-minus-Hankel matrix and possesses all the nice properties that were described in Section 3. Let  $\nu_j, j = 1, \dots, M$ , be its eigenvalues and  $\mathbf{w}^j = (w_1^j, w_2^j, \dots, w_M^j)^T$  be the corresponding orthonormal eigenvectors. Moreover, let  $W$  be the  $M \times M$  orthogonal matrix  $W = (\mathbf{w}^1, \mathbf{w}^2, \dots, \mathbf{w}^M)$ , and  $s_j$  be the trigonometric polynomial

$$s_j(x) = \sum_{i=1}^M w_i^j X_i(x), \quad j = 1, 2, \dots, M, \quad (28)$$

where  $w_i^j$  are as above.

Next, we project the array response matrix  $\widehat{\Pi}$  on the  $M$  trigonometric polynomials  $s_n$ , rather than on the first  $M$  vertical eigenfunctions  $X_n$ . Specifically, let  $\widehat{\mathbb{S}}$  be the  $M \times M$  matrix with entries

$$\widehat{\mathbb{S}}_{mn} = \frac{1}{\nu_m \nu_n} \int_{\mathcal{A}} dx_s \int_{\mathcal{A}} dx_r \widehat{\Pi}(\vec{x}_s, \vec{x}_r, \omega) s_m(x_s) s_n(x_r), \quad (29)$$

where  $m, n = 1, \dots, M$ . It is immediate to verify that

$$\int_{\mathcal{A}} s_k(x) X_m(x) dx = \nu_k w_m^k, \quad k, m = 1, \dots, M. \quad (30)$$

Replacing (12) and (28) into (29), and in view of (30), we arrive at the following matrix identity

$$\widehat{\mathbb{S}} = -\frac{1}{4} W^T D_\beta Q A_M Q D_\beta W. \quad (31)$$

As a final step, note that  $W$  is an orthogonal matrix hence if we define

$$\widehat{\mathbb{P}} = D_\beta^{-1} W \widehat{\mathbb{S}} W^T D_\beta^{-1}. \quad (32)$$

we may check that

$$\widehat{\mathbb{P}} = -\frac{1}{4} D_\beta^{-1} \underbrace{W W^T}_{I_M} D_\beta Q A_M Q D_\beta \underbrace{W W^T}_{I_M} D_\beta^{-1} = -\frac{1}{4} Q A_M Q. \quad (33)$$

So, by following the steps described above, one may end up with a matrix  $\widehat{\mathbb{P}}$  that (up to the multiplicative constant  $-1/4$ ) is unitarily equivalent to  $A_M$ . Let us also note that in the full array case the orthonormality of the  $X_n$ 's implies that  $A_{\text{arr}}$  is the identity matrix,  $s_j(x) = X_j(x)$  and  $W = I_M$ , thus we recover the previous definition of  $\widehat{\mathbb{P}}$ , see (7).

#### 4.2. Implementation aspects

We feel that the previous approach may be useful for theoretical purposes mainly. The main reason for that hinges on the fact that the data that we have in our disposal is the  $N^2$  values tabulated in  $\widehat{\Pi}$ . Hence the integrals over  $\mathcal{A}$  in (30) have to be evaluated numerically whereas the validity of (33) relies crucially on the fact that (30) holds. In practice, (30) holds only approximately due to inherent errors in the course of numerical integration; as a result those errors 'pollute' (33) as well.

In order to avoid these difficulties we propose the following implementation of our method in order to work on the matrix level. To this end we consider the real, symmetric matrix  $h(V^T V)$ , where  $V$  is the  $N \times M$  matrix defined in (15). Let, also,  $S$  be the  $M \times N$  matrix with  $S_{ij} = s_i(x_j)$ ,  $i = 1, \dots, M$ ,  $j = 1, \dots, N$ , where  $s_i(x_j)$  is the  $i$ -th trigonometric polynomial defined in (28) evaluated at the depth of the  $j$ -th transducer. Now, by abusing slightly the notation,  $\nu_j$  and  $\mathbf{w}^j = (w_1^j, w_2^j, \dots, w_M^j)^T$  are the eigenvalues and corresponding orthonormal eigenvectors of the Gram matrix  $h(V^T V)$ . Notice that the scaling factor  $h$  is used here just to push the  $\nu_i$ 's to cluster near one and zero (instead of near  $h^{-1}$  and zero) as we shall see later.

It is easy to show that

$$SV = h^{-1}D_\nu W^T, \quad \text{where } D_\nu = \text{diag}(\nu_1, \dots, \nu_M),$$

(a matrix equivalent of (30)), and since  $W$  is orthogonal we deduce that

$$WD_\nu^{-1}SV = h^{-1}I_M$$

Therefore, if we define the matrix  $\hat{\mathbb{P}}$  as

$$\hat{\mathbb{P}} = D_\beta^{-1} W D_\nu^{-1} S \hat{\Pi} S^T D_\nu^{-1} W^T D_\beta^{-1},$$

we get that

$$\hat{\mathbb{P}} = -\frac{1}{4}D_\beta^{-1} \underbrace{W D_\nu^{-1} S V D_\beta Q A_M Q D_\beta}_{h^{-1}I_M} \underbrace{V^T S^T D_\nu^{-1} W^T}_{h^{-1}I_M} D_\beta^{-1} = -\frac{1}{4h^2}Q A_M Q,$$

so  $\hat{\mathbb{P}}$  is again unitarily equivalent to  $A_M$  (up to the multiplicative constant  $-1/(4h^2)$ ).

We summarize these in the following definition

**Definition 4.1** *Given the array response matrix  $\hat{\Pi}$  for the scattered field, we first consider the  $M \times N$  matrix*

$$\tilde{S} = D_\nu^{-1} S, \tag{34}$$

where

$$S_{ij} = s_i(x_j), \quad i = 1, \dots, M, \quad j = 1, \dots, N, \quad \text{and } D_\nu = \text{diag}(\nu_1, \dots, \nu_n),$$

and next, we define  $\hat{\mathbb{P}}$  by

$$\hat{\mathbb{P}} = D_\beta^{-1} W \tilde{S} \hat{\Pi} \tilde{S}^T W^T D_\beta^{-1}. \tag{35}$$

Then we use  $\hat{\mathbb{P}}$  in  $\tilde{\mathcal{I}}^{\text{KM}}$  (as defined in (6)), i.e.,

$$\tilde{\mathcal{I}}^{\text{KM}}(\vec{y}^s, \omega) = -\frac{1}{4h^2} \sum_{m,n=1}^M e^{-i(\beta_m + \beta_n)|z_a - z^s|} X_n(x^s) X_m(x^s) \hat{\mathbb{P}}_{mn}(\omega),$$

for imaging.

In order to assess the performance of  $\tilde{\mathcal{I}}^{\text{KM}}$ , as defined above, we apply our methodology in the test case that we have considered in the beginning of the present section. In the leftmost subplot of Figure 6 we show  $\tilde{\mathcal{I}}^{\text{KM}}$  images for full array, while the other three subplots correspond to array lengths  $l_{\text{arr}} = 180, 140, 100$  m, respectively. In all cases the length of the array is reduced symmetrically from both ends.

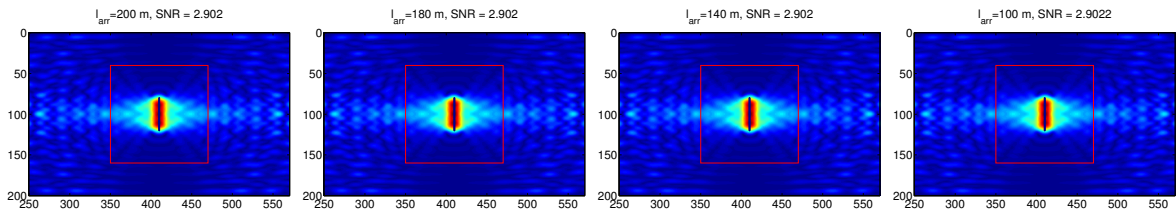


Figure 6: Imaging with  $\tilde{\mathcal{I}}^{\text{KM}}$  for the screen, when  $l_{\text{arr}} = 200, 180, 140, 100$  m, for  $f = 73$  Hz.

Next, in Figure 7, we plot selective imaging results obtained with the functional  $\tilde{\mathcal{I}}_J^{\text{KM}}$ , for  $J = 1, 2, 3, 4$ , when  $l_{\text{arr}} = 180$  m. Selective imaging with  $\tilde{\mathcal{I}}_J^{\text{KM}}$  performs as if we were using the full-aperture array; all four images are very good with high SNR  $> 1.9$ , and projection on the first singular vector results in focusing on the middle of the screen while projection on the second to fourth singular vectors provides information about the location of its edges. These images remain identical until we reduce by half the length of the array (symmetrically from both ends).

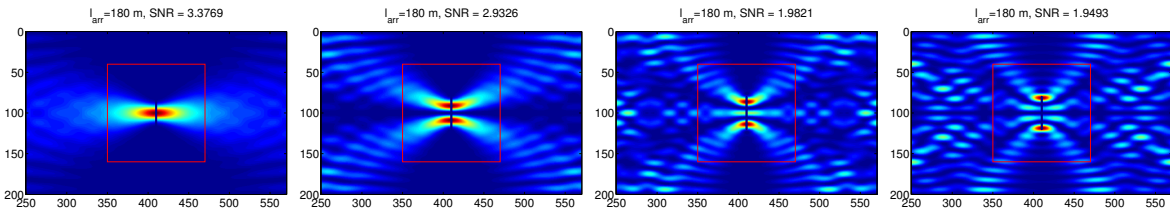


Figure 7: Imaging with  $\tilde{\mathcal{I}}_J^{\text{KM}}$  for the screen, for  $J = 1, 2, 3, 4$  when  $l_{\text{arr}} = 180$  m, for  $f = 73$  Hz.

The results in Figures 6, 7 are in perfect agreement with the theory in this ideal case; they are excellent and in some sense counter intuitive, since there is no loss of information despite the fact that we decrease the array length. Note that this is certainly not true for the functional that we have used to create the images in Figure 5, where the quality of the images deteriorates as the array aperture decreases.

### 4.3. Numerical experiments: Partial-aperture array imaging for the model problem

**4.3.1. The noiseless data case** So far we have seen that for the screen model problem and under the assumption that all arithmetic operations are exact (i.e. they are performed with infinite precision), the spectral properties of  $\hat{\mathbb{P}}$  (as defined by (35)) are determined by those of  $A_M$ , thus we expect  $\tilde{\mathcal{I}}^{\text{KM}}$  to perform in exactly the same way as if we were using a full-aperture array. However, in practice we use finite precision arithmetic so we have to examine whether and how this affects the performance of our method.

A quite obvious cause of potential numerical instabilities is the presence of the reciprocals  $\nu_i^{-1}$  of the eigenvalues of the matrix  $h(V^T V)$  in the definition of  $\tilde{S}$ , see (34). Hence it is important to examine the behavior of the  $\nu_i$ 's, and how it is related to the length of the array  $\mathcal{A}$ . An important remark in this direction is that  $h(V^T V)$  may be considered as an approximation of the  $M \times M$  matrix Toeplitz-minus-Hankel matrix  $A_{\text{arr}}$ . Therefore we would expect  $\nu_i$  to cluster near 0 and 1 and, specifically, roughly  $[l_{\text{arr}}/(\lambda/2)]$  of them to lie near 1, and the rest  $M - [l_{\text{arr}}/(\lambda/2)]$  to approach zero. Moreover, as  $l_{\text{arr}}$  decreases, more singular values tend to zero, and in fact  $h(V^T V)$  will become practically singular as soon as its minimum eigenvalue  $\nu_{\min}$  falls below a certain threshold.

In some cases there do exist theoretical bounds for the minimum eigenvalues of Toeplitz matrices. For example, Serra in [30] shows that if  $T$  is an  $(n + 1) \times (n + 1)$  Toeplitz matrix with generating function a real integrable function on  $[-\pi, \pi]$ , which is strictly positive in a closed interval  $J \subset I$  and zero elsewhere, then for  $n$  sufficiently large, and for any  $\epsilon \in (0, t)$ , its minimum eigenvalue  $\lambda_{\min}$  is bounded as

$$c_1 (t - \epsilon)^{n(n+1)/2} < \lambda_{\min} < c_2 t^n,$$

where  $c_1, c_2$  are positive constants (independent of  $n$ ), and  $t$  is a constant less than one that depends on the width of the interval  $J$ ; specifically  $t = \sin^2(|J|/4)$ , see also [28]. In our case, we may apply these bounds in the case where the array is attached on the top of the waveguide. Then the generating function of the Toeplitz-minus-Hankel matrix  $A_{\text{arr}}$  is the indicator function  $\mathbb{1}_{\tilde{J}}(x)$  of  $\tilde{J} = [-l_{\text{arr}}, l_{\text{arr}}]$ , and the minimum eigenvalue of  $A_{\text{arr}}$  is equal to the minimum odd eigenvalue of its associated  $(2M + 1) \times (2M + 1)$  Toeplitz counterpart. Hence, we expect its minimum eigenvalue to decrease to zero like  $\tau^{2M}$ , where

$$\tau = \sin^2\left(\frac{\pi l_{\text{arr}}}{2D}\right).$$

As already said, we expect that the eigenvalues of  $h(V^T V)$  behave like those of  $A_{\text{arr}}$ . In Figure 8 we plot (using a logarithmic scale on the vertical axis) the minimum eigenvalue  $\nu_{\min}$  of the  $M \times M$  matrix  $h(V^T V)$  (computed in MATLAB) and the values predicted by the bounds  $\tau^{2M}$  and  $\tau^{2M(2M+1)/2}$  as  $l_{\text{arr}}$  decreases. As an indication of the relative error due to floating point arithmetic we use the so-called machine epsilon  $\epsilon$  (implemented in MATLAB and printed as a blue dashed line in the figure). Here, the frequency  $f = 73$  Hz,  $D = 200$  m, thus  $M = 19$  modes propagate, and the array pitch is  $h = 2.5$  m  $\simeq \lambda/8$ . The results shown in Figure 8 suggest that the minimum eigenvalue of  $h(V^T V)$  drops below  $\epsilon$  when the length of the array is less than 120 m.

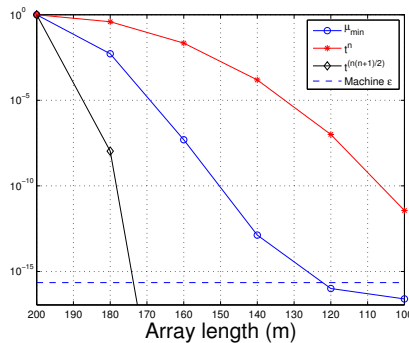


Figure 8: The minimum eigenvalue of  $h(V^T V)$  (blue circles) vs.  $\tau^n$  (red asterisks) and  $\tau^{n(n+1)/2}$  (black diamonds) for  $f = 73$  Hz and  $n = 2M$ , when we decrease the length of the array from below.

In Figure 9 we plot the minimum eigenvalue of  $h(V^T V)$  as we decrease  $l_{\text{arr}}$  and for various values of the array pitch  $h$ . In the left subplot the length of the array is reduced

symmetrically with respect to the mid-depth of the waveguide, while in the right one the lower part of the array is cut off. The different markers (also typed in different colors) shown in Figure 9 correspond to arrays with different densities; the value of  $h$  that corresponds to each marker is reported in the legend of the figure in terms of the reference wavelength  $\lambda_0 = 20$  m. We observe that the decay rate is much faster in the non-symmetric case (right subplot) than in the symmetric one (left). Moreover, the density of the array seems to affect the rate at which  $\nu_{\min}$  drops below  $\varepsilon$ ; these results indicate that the magnitude of  $\nu_{\min}$  is stabilized with an inter-element array distance of approximately  $\lambda_0/8$ .

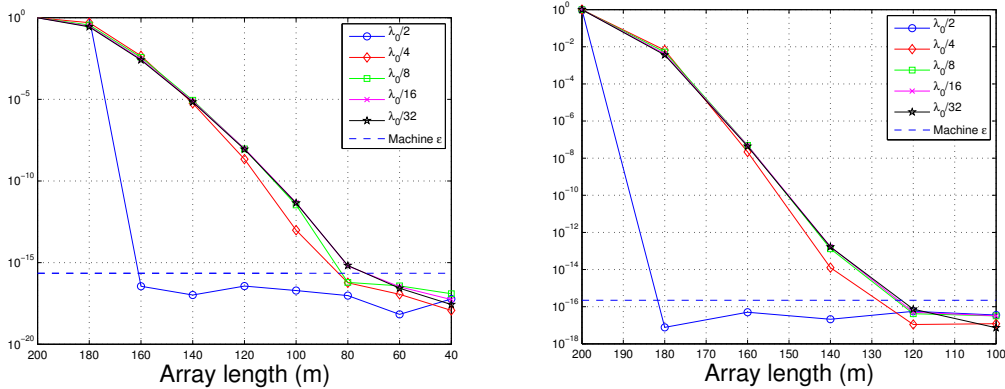


Figure 9: Behavior of  $\nu_{\min}$  when we decrease the length of the array symmetrically from both ends (left subplot) and just from below (right subplot), for  $f = 73$  Hz.

By inspecting the plots in Figure 9 we expect no loss in image resolution or signal to noise ratio (SNR) in our images with  $\tilde{\mathcal{I}}^{\text{KM}}$  as long as  $\nu_{\min}$  stays above some threshold  $\varepsilon^+$ . However, as  $\nu_{\min}$  approaches machine  $\varepsilon$ , most likely one will experience numerical instabilities. As a regularization procedure we may try the following filtering: Consider some threshold  $\varepsilon^+$ . Then if  $\nu_c > \varepsilon^+ > \nu_{c+1}$ , for some  $c \in \{1, \dots, M\}$ , we set  $1/\nu_i = 0$ , for  $i \geq c+1$ . Notice that the reciprocals  $\nu_i^{-1}$  of these small eigenvalues, which are in fact very big, multiply the lower  $(M-c) \times N$  part of the matrix  $S$ ; let us call it  $S_c$ . Intuitively we expect the entries of  $S_c$  to be very small since, for example, the  $j$ -th row contains the values of the trigonometric polynomial  $s_j$  calculated on the receivers' depths, and recall that our results in Section 3 suggest that when  $\nu_j$  is small then  $s_j$  is mainly supported on the exterior of  $\mathcal{A}$  (see, for example, Figures 3 and 4 that exhibit the behavior of the trigonometric polynomials with coefficients the eigenvectors of the matrix  $A_M$  defined in (16), and recall that the matrix  $h(V^T V)$  approximates  $A_{\text{arr}}$  defined in (27) which is of the same form as  $A_M$ ). Indeed, one may prove that  $\|S_c\|_{\text{F}}^2 = (\sum_{i=c+1}^M \nu_i)/h < (M-c)\varepsilon^+/h$ , where  $\|\cdot\|_{\text{F}}$  is the Frobenius matrix norm, to give grounds to the proposed regularization technique. Of course, in the case we employ this filtering technique we do not expect a unitary equivalence relation between  $\hat{\mathbb{P}}$  and  $A_M$  to hold any more.

We clarify the above by giving some examples. We decrease the length of the array at  $l_{\text{arr}} = 60$  m (symmetrically from both ends), i.e. the array covers 30% of

the waveguide depth. In order to form  $\widehat{\mathbb{P}}$  we use a threshold  $\varepsilon^+ = 10^{-15}$  that forces the reciprocals of the last three eigenvalues of  $h(V^T V)$  to be equal to zero. One may verify the good quality of the image shown on the top right corner of Figure 10 that is obtained with the proposed filtering. On the top left corner we plot the singular values of  $\widehat{\mathbb{P}}$ . The bottom row in Figure 10 shows the corresponding results when we do not use any filtering and demonstrates the catastrophic effect of roundoff errors during the computation of  $\widehat{\mathbb{P}}$ .

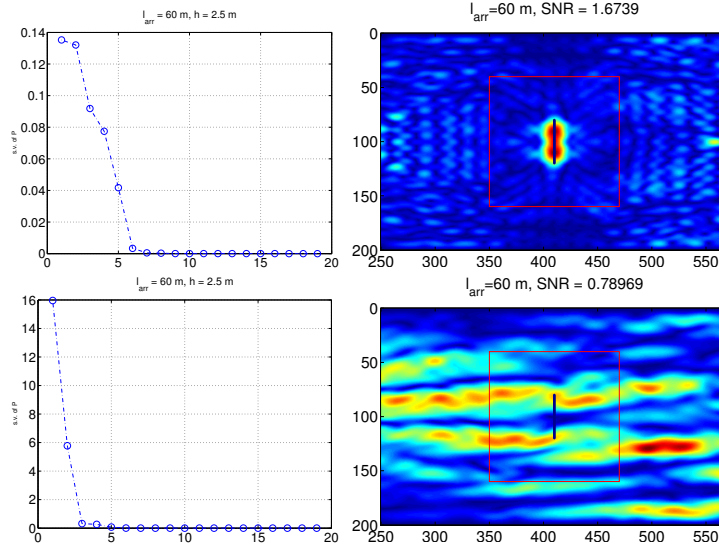


Figure 10: Top: The singular values of  $\widehat{\mathbb{P}}$  (left) and the associated  $\widetilde{\mathcal{I}}^{\text{KM}}$  image (right) that we obtain with threshold  $\varepsilon^+ = 10^{-15}$ . Bottom: The same as in the top row but without using  $\varepsilon^+$ . Here  $l_{\text{arr}} = 60$  m,  $h = \lambda_0/8$  and  $f = 73$  Hz.

Figure 11 depicts selective imaging results with  $\widetilde{\mathcal{I}}_J^{\text{KM}}$ , where again in the course of constructing  $\widehat{\mathbb{P}}$  we employ the threshold  $\varepsilon^+ = 10^{-15}$ . Here, selective imaging with  $\widetilde{\mathcal{I}}_J^{\text{KM}}$  fails, in the sense that the usual ordering in focusing does not hold anymore. To be precise, this means that we lose the property that when we project on the singular vector that corresponds to the largest singular value we get an image that provides information about the bulk of the object, while projection on the singular vectors that correspond to smaller singular values carry information about its edges. This is something to be expected since filtering prevents to establish a unitary equivalence relation between  $\widehat{\mathbb{P}}$  and  $A_M$ . However, the images for  $J = 2, 3$  and 4 still have good SNR and provide useful information about the object.

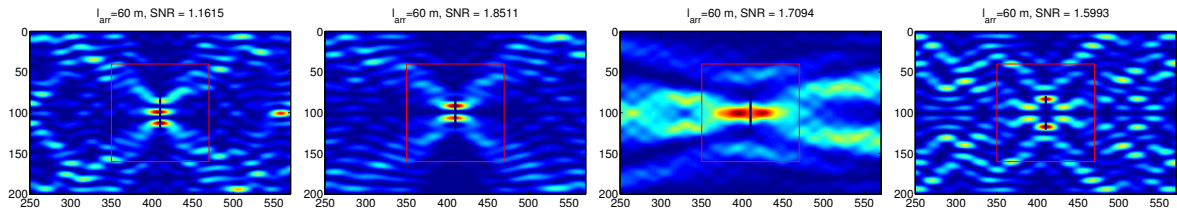


Figure 11: Imaging with  $\tilde{\mathcal{I}}_J^{\text{KM}}$  for the screen with  $\varepsilon^+ = 10^{-15}$ , for  $J = 1, 2, 3, 4$ , when  $l_{\text{arr}} = 60$  m, for  $h = \lambda_0/8$  and  $f = 73$  Hz.

In order to push  $\tilde{\mathcal{I}}^{\text{KM}}$  to the limit for this model problem we decrease (symmetrically) the length of the array to be equal to  $l_{\text{arr}} = 20$  m (this is just 10% of the total waveguide depth). In this case, we make the array denser by setting the pitch  $h = \lambda_0/20 = 1.0$  m. The image shown in Figure 12 is generated with a threshold equal to  $\varepsilon^+ = 10^{-15}$  that removes the reciprocals of the last 8 singular values of  $h(V^T V)$ . We observe that the  $\tilde{\mathcal{I}}^{\text{KM}}$  image gives us very good information about the object, although its SNR value is quite low, about 1.2, due to the presence of the small artifact that is visible on the right side of the image.

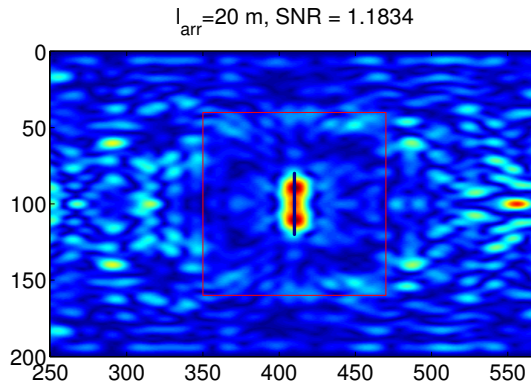


Figure 12: Imaging with  $\tilde{\mathcal{I}}^{\text{KM}}$  for the screen with  $\varepsilon^+ = 10^{-15}$  when  $l_{\text{arr}} = 20$  m, for  $h = \lambda_0/20$  and  $f = 73$  Hz.

We close this paragraph with a few remarks.

**Remark 2** (i) In all results that we have shown thus far we have reduced the length of the array symmetrically from both ends and we have placed the screen centered in the mid-depth of the waveguide. We have experimented with various other configurations altering the way we reduce the array and/or the position of the screen. Our results suggest that in some cases we may have to use filtering for larger array lengths than before. For example, when we reduce the length of the array from below the eigenvalues of  $h(V^T V)$  decrease towards zero much faster, see Figure 9, and indeed in this case we have to employ some threshold  $\varepsilon^+$  for larger arrays than those reported in the examples shown here.

- (ii) One may try different approaches to construct a weighted projection of the array response matrix in the partial array case. For example, we may define  $\widehat{\mathbb{P}} = D_\beta^{-1} V^+ \widehat{\Pi} (V^T)^+ D_\beta^{-1}$ , where  $V^+$  is the Moore-Penrose pseudoinverse of  $V$ . Then it is immediate to check that in the screen model problem, and under the assumption that all computations are performed with infinite precision,  $\widehat{\mathbb{P}}$  is unitarily equivalent to  $A_M$ . However, as we decrease the length of the array we still have to use a regularized pseudoinverse that treats as zero any singular values of  $V$  less than some suitable threshold.
- (iii) So far we have seen that when we decrease  $l_{\text{arr}}$  beyond some level and we employ some thresholding to the  $\nu_i^{-1}$  the nice ‘ordering’ property of the selective imaging functional  $\widetilde{\mathcal{I}}_J^{\text{KM}}$  does not hold. However, in a post-processing stage, one may still have some benefit in imaging using the functional  $\widetilde{\mathcal{I}}^{\text{KM},\text{f}}$ , see (9), where in the filtered version of  $\widehat{\mathbb{P}}$  we may take into account those of its singular vectors that correspond to ‘good’  $\widetilde{\mathcal{I}}_J^{\text{KM}}$  images.

4.3.2. *Adding noise to the data* In the previous subsection, we found that  $\widetilde{\mathcal{I}}^{\text{KM}}$  seems to work very well under ideal conditions that allow us to derive  $\widehat{\Pi}$  analytically in the special form (13). Now we shall examine the performance of our method under the effect of measurement noise. Specifically, we model measurement noise, as in [6], adding a noise matrix  $W(\omega)$  with zero mean uncorrelated Gaussian distributed entries with variance  $\epsilon p_{\text{avg}}$ , i.e.  $W_{r,s}(\omega) \sim \mathcal{N}(0, \epsilon p_{\text{avg}})$ . Here the average power received per source and receiver is given by

$$p_{\text{avg}} = \frac{1}{N^2} \|\widehat{\Pi}(\omega)\|_{\text{F}}^2,$$

where  $\|\cdot\|_{\text{F}}$  is the Frobenius matrix norm. The expected power of the noise  $W(\omega)$  over all receivers and sources is

$$\mathbb{E} [\|W(\omega)\|_{\text{F}}^2] = \epsilon N^2 p_{\text{avg}}.$$

Since the total power of the signal received over all receivers and sources is  $N^2 p_{\text{avg}}$ , the Signal-to-Noise Ratio (SNR) in dB is  $-10 \log_{10} \epsilon$ .

In Figure 13 we superimpose the singular values of  $\widehat{\Pi}$  and  $\widehat{\Pi} + W$  when we add noise of 10 dB to our data, and the array is reduced symmetrically to have length equal to  $l_{\text{arr}} = 140$  m. We use a linear scale for the  $y$ -axis in the left subplot and a  $\log_{10}$  scale in the right one. As one may immediately verify the largest singular values of  $\widehat{\Pi} + W$  remain close to those of  $\widehat{\Pi}$ , while the noise severely affects the smaller ones.

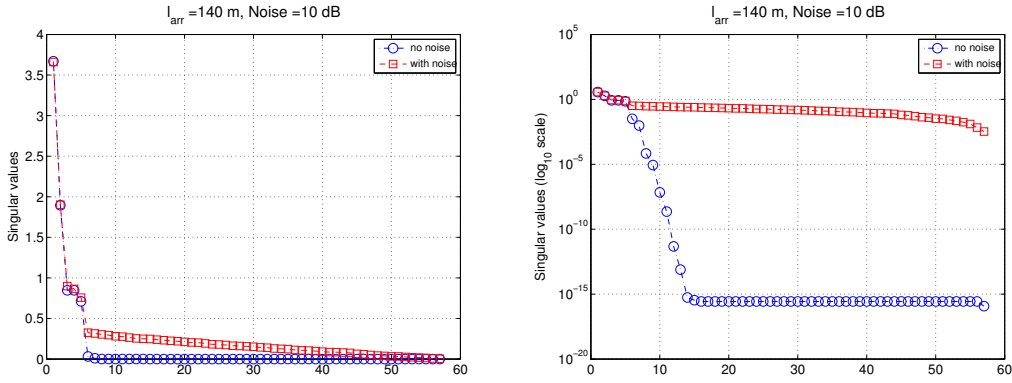


Figure 13: The singular values of  $\hat{\Pi}$  and  $\hat{\Pi} + W$  using a linear scale for the  $y$ -axis (left) and a  $\log_{10}$  scale (right). Here  $l_{\text{arr}} = 140$  m and  $f = 73$  Hz.

Next, we present the outcome of some of the experiments that we have performed with 10 dB SNR, keeping the rest of the parameters the same as in the previous sections. We begin with an array with  $l_{\text{arr}} = 140$  m. In Figure 14 we plot the singular values of  $h(V^T V)$  using a linear scale for the vertical axis in the left subplot and a  $\log_{10}$  scale in the right one. Note that the smallest singular value is greater than  $10^{-6}$ , hence all the singular values of  $h(V^T V)$  are well above the threshold  $\varepsilon^+ = 10^{-15}$  that we have used so far. However, as one may see in the top left subplot of Figure 15 the SVD of  $\hat{\mathbb{P}}$  does not follow the usual pattern. Specifically, the first singular value of  $\hat{\mathbb{P}}$  is 133.2, the second 57.9, while the rest are less than 1. This is an indication that something goes wrong and, indeed, the corresponding image shown in the bottom left subplot is just noise. In order to improve this unsatisfactory result we employ some threshold  $\varepsilon^+$  during the computation of  $S$  in order to remove gradually those  $\nu_i^{-1}$  that correspond to the smaller  $\nu_i$ 's, one at a time. The  $\tilde{\mathcal{I}}^{\text{KM}}$  images obtained by removing those  $\nu_i^{-1}$  that correspond to the smallest one, or two,  $\nu_i$  are also very bad and we do not show them here. In the middle subplots of Figure 15 we present the singular values of  $\hat{\mathbb{P}}$  (top) and the corresponding  $\tilde{\mathcal{I}}^{\text{KM}}$  image (bottom) for a threshold  $\varepsilon^+ = 10^{-2}$ ; with this value we treat as zero the  $\nu_i^{-1}$  that correspond to the smaller three  $\nu_i$ 's, see Figure 14. Things are also well by choosing  $\varepsilon^+ = 5 \cdot 10^{-2}$ , thus setting one more  $\nu_i^{-1}$  equal to zero.

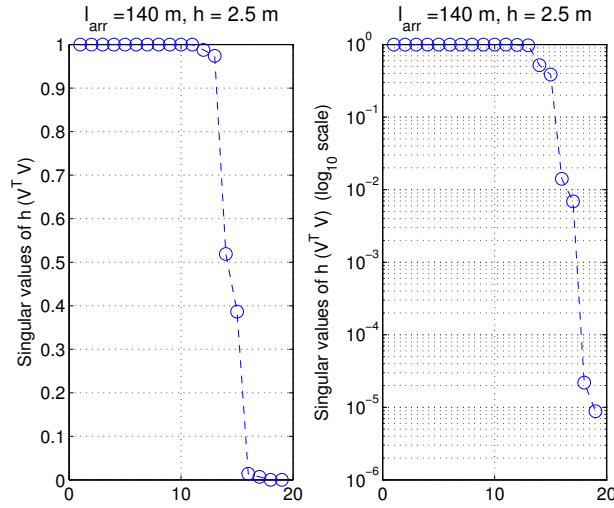


Figure 14: The singular values of  $h(V^T V)$  using a linear scale for the  $y$ -axis (left) and a  $\log_{10}$  scale (right). Here  $l_{\text{arr}} = 140$  m and  $f = 73$  Hz.

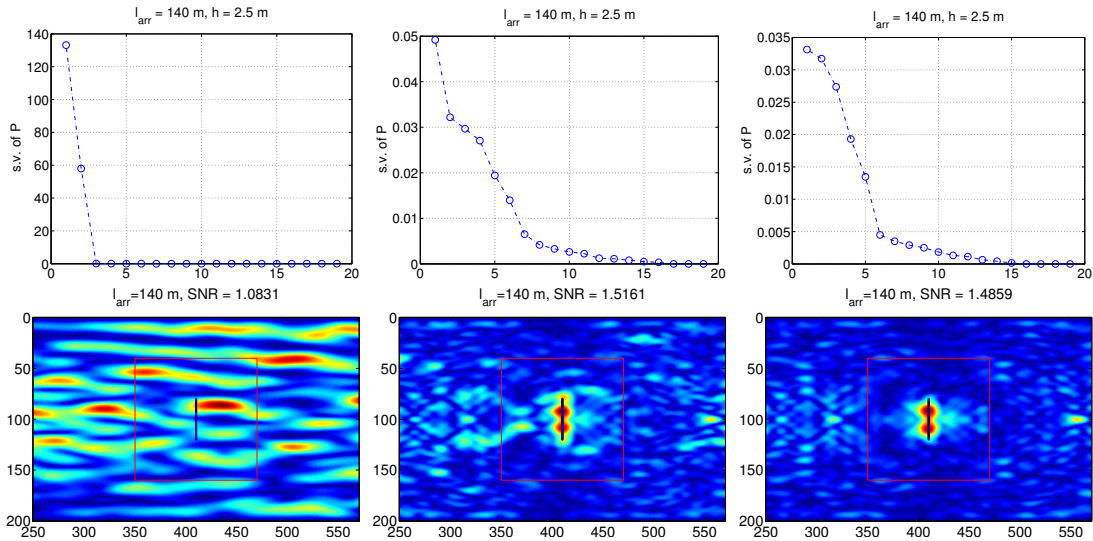


Figure 15: Singular values of  $\widehat{\mathbb{P}}$  (top row) and  $\widetilde{\mathcal{I}}^{\text{KM}}$  images (bottom row) for the screen, without a threshold (left subplots) and with a threshold  $\varepsilon^+ = 10^{-2}$  that removes 3 (middle subplots) and  $\varepsilon^+ = 5 \cdot 10^{-2}$  that removes 4 (right subplots) of the smallest  $\nu_i^{-1}$ , respectively (compare with Figure 14).  $l_{\text{arr}} = 140$  m, and  $f = 73$  Hz.

Looking once again at Figure 14, and recalling the results of Section 3, we realise that the choice of the threshold value  $\varepsilon^+ = 5 \cdot 10^{-2}$  does in fact dictate to project the array response matrix  $\widehat{\Pi}$  just on the trigonometric polynomials that are supported on  $\mathcal{A}$ ; also recall that their number is expected to be roughly  $l_{\text{arr}}/(\lambda/2)$ . Keeping this in mind, we next examine whether in order to obtain good images for various lengths of the array it suffices to compute  $\widehat{\mathbb{P}}$  using a threshold  $\varepsilon^+$  that excludes those trigonometric

polynomials with coefficients the eigenvectors of  $A_{\text{arr}}$  that belong to the noise subspace; these are supported on the exterior of  $\mathcal{A}$ . To this end, we plot in Figure 16 the singular values of  $h(V^T V)$  (top line) and the corresponding  $\tilde{\mathcal{I}}^{\text{KM}}$  images (bottom line) for the screen, with  $l_{\text{arr}} = 120$  m (left subplots),  $l_{\text{arr}} = 100$  m (middle subplots), and  $l_{\text{arr}} = 90$  m (right subplots). In all cases we take  $\varepsilon^+ = 5 \cdot 10^{-2}$  that removes 6, 8 and 8 of the smallest  $\nu_i^{-1}$ , respectively. As one may see, and as it is expected, the quality of the images deteriorates as we decrease the length of the array but it remains acceptable even if we place symmetrically in the waveguide an array that covers more or less the half of its depth.

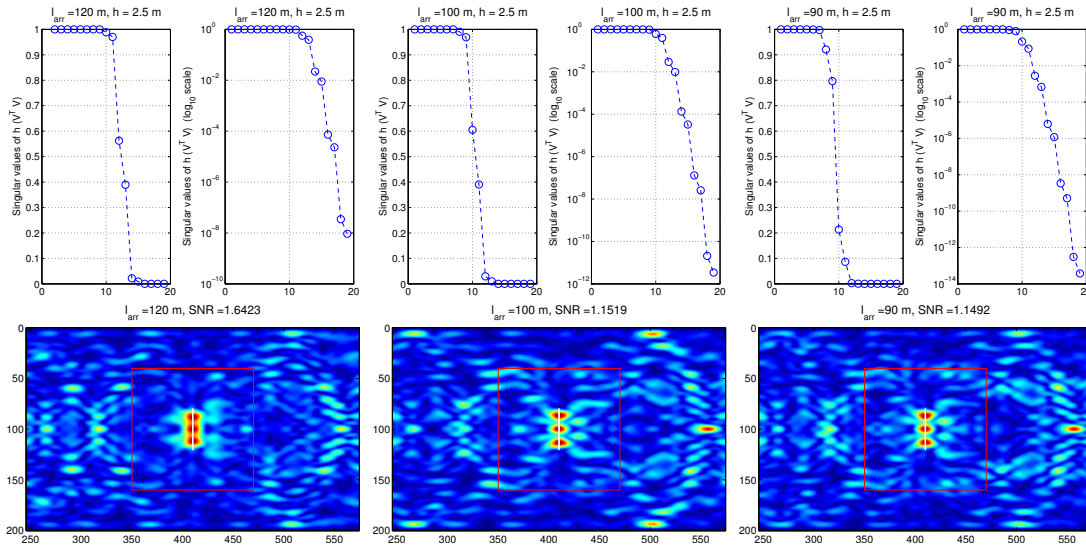


Figure 16: Singular values of  $h(V^T V)$  (top row) and  $\tilde{\mathcal{I}}^{\text{KM}}$  images (bottom row) for the screen, with  $l_{\text{arr}} = 120$  m (left subplots),  $l_{\text{arr}} = 100$  m (middle subplots), and  $l_{\text{arr}} = 90$  m (right subplots). In all cases  $\varepsilon^+ = 5 \cdot 10^{-2}$  that removes 6, 8 and 8 of the smallest  $\nu_i^{-1}$ , respectively.

Finally, on both subplots of Figure 17, instead of using the whole matrix  $\hat{\mathbb{P}}$ , as it is obtained with thresholding with  $\varepsilon^+ = 5 \cdot 10^{-2}$ , we project on certain of its singular vectors. On the left subplot  $l_{\text{arr}} = 100$  m and we project on the second and third singular vectors of  $\hat{\mathbb{P}}$ , while on the right one  $l_{\text{arr}} = 90$  m and we project just on the second singular vector. Both images exhibit better SNR compared to their counterparts in Figure 16, albeit with a worse range resolution.

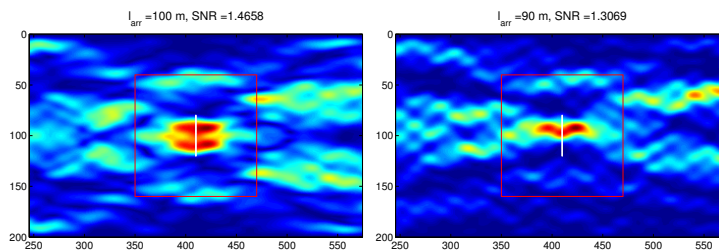


Figure 17:  $\tilde{\mathcal{I}}^{\text{KM},f}$  images for the screen, with  $l_{\text{arr}} = 100$  m where we project on the second and third singular vectors of  $\hat{\mathbb{P}}$  (left subplot) and  $l_{\text{arr}} = 90$  m where we project on the second singular vector. In both cases  $\hat{\mathbb{P}}$  was derived with  $\varepsilon^+ = 5 \cdot 10^{-2}$ .

## 5. Numerical experiments

So far we have seen that the proposed definition of the projected array response matrix  $\hat{\mathbb{P}}$ , see (35), leads to excellent imaging results in the ideal screen model problem even for very small arrays. Of course, one may reasonably argue that this method is tailored to that specific model problem, hence it is natural to ask how it performs when applied in situations that deviate from the previously described ideal setting. To this end, in the present section, we assess the performance of  $\tilde{\mathcal{I}}^{\text{KM}}$  with partial information for a scatterer that is either square- or disc-shaped. Moreover, the array response matrix for the scattered field  $\hat{\Pi}^{\text{sc}}$  is computed numerically by solving the full wave equation (1) supplemented with appropriate initial and boundary conditions, with the aid of Montjoie [22], a high-order finite element C++ code developed at INRIA.

We truncate the infinite in range waveguide with two perfectly matched layers (PML) [3, 12], see Figure 18. One near the source ranging between  $-100$  and  $0$  m, and the other far from the source between  $500$  and  $600$  m. We found that the  $100$  m PML width was effective to absorb outgoing waves at least for the frequency range that we used. We discretize the resulting computational domain with quadrangles on which the usual basis functions of the  $\mathbb{Q}_n$  family ( $\mathbb{Q}_n = \text{span}\{x^\ell y^m, 0 \leq \ell, m \leq n\}$ ) are used. Specifically, we use  $\mathbb{Q}_8$  polynomials for the square scatterer, and  $\mathbb{Q}_{12}$  for the disc. Numerical quadrature is based on Gauss-Lobatto rules, and for time discretization we employ a fourth-order Leap-Frog scheme.

The array imaging setup is similar to the one used in the previous section, with the exception that now our vertical array is placed at  $z_a = 40$  m, has a pitch  $h = 5$  m and spans the whole depth of the waveguide. Then we extract the array response matrix for the partial array by removing appropriate lines and columns from the matrix that corresponds to the full aperture array. The results shown in this section regard an array that its length is reduced symmetrically from both ends, and a scatterer that is centered in the mid-depth of the waveguide.

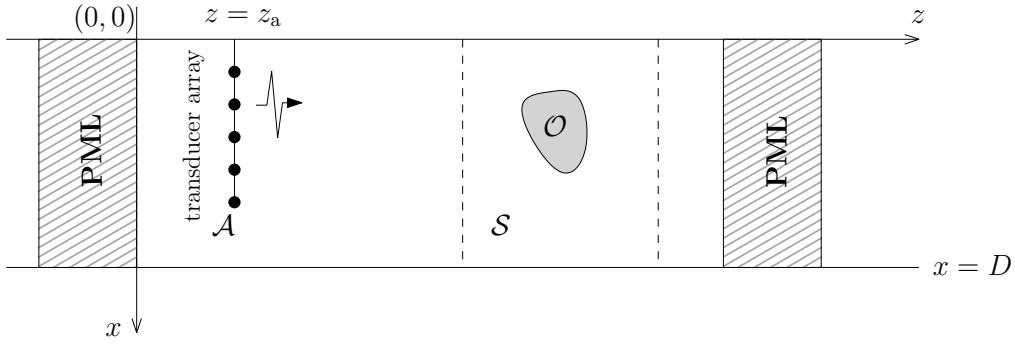


Figure 18: Sketch of a waveguide that is truncated near and far from the source with two PML.

### 5.1. Constant sound speed

To begin with, we consider a constant sound speed  $c_0 = 1500$  m/s, and we assume that the length of the array equals  $l_{\text{arr}} = 180$  m. The singular values of  $h(V^T V)$  are shown in the left subplot of Figure 19. They are all larger than 0.5 thus suggesting that there is no need to employ some threshold in the computation of  $\tilde{S}$ . Indeed, the  $\tilde{\mathcal{I}}^{\text{KM}}$  images for the square and the disc, that are shown in the middle and right subplots of Figure 19, respectively, are both very good. The image for the square reconstructs the left side of the scatterer, while for the disc it mainly focuses around the left endpoint of its horizontal diameter.

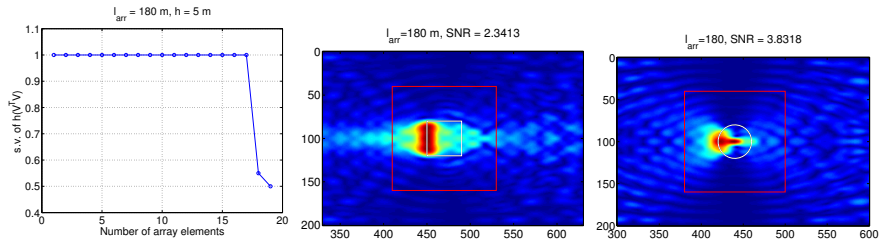


Figure 19: Singular values of  $h(V^T V)$  (left), imaging with  $\tilde{\mathcal{I}}^{\text{KM}}$  for the square (middle) and the disc (right), when  $l_{\text{arr}} = 180$  m, for  $f = 73$  Hz.

In Figure 20, we present selective imaging results with  $\tilde{\mathcal{I}}_j^{\text{KM}}$  for the square on the top row, and for the disc on the bottom row. The images are very similar to the corresponding ones for a full array, and these for the square-shaped scatterer compare very well with those we have seen for the screen model problem in Figure 7.

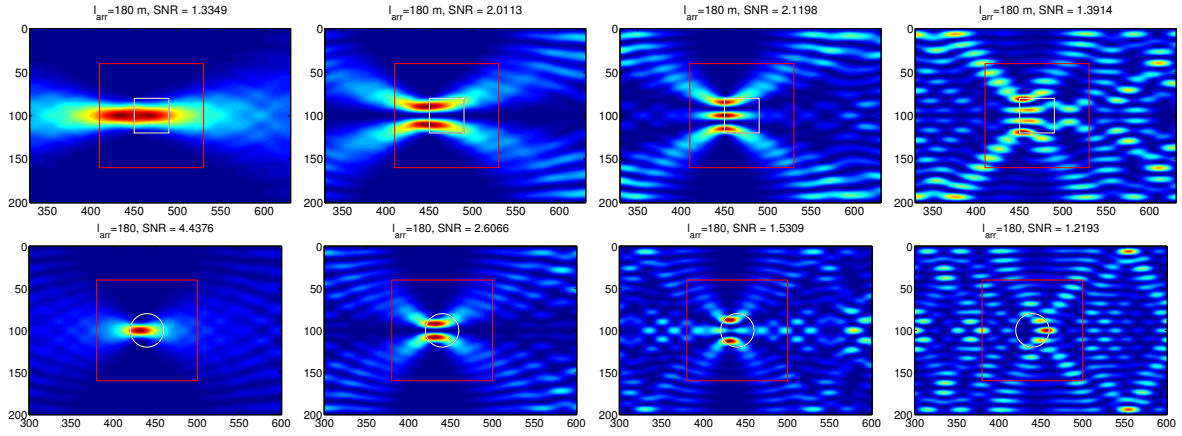


Figure 20: Imaging with  $\tilde{\mathcal{I}}_J^{\text{KM}}$  for the square (top) and the disc (bottom), for  $J = 1, 2, 3, 4$  when  $l_{\text{arr}} = 180$  m, for  $f = 73$  Hz.

To work with smaller arrays it emerges the need of imposing a threshold  $\varepsilon^+$  in the course of computing  $\tilde{S}$ . All results that we present in the remaining of this subsection were derived with  $\varepsilon^+ = 0.02$ , which practically means that we project the array response matrix  $\hat{\Pi}$  just on the trigonometric polynomials that are supported on  $\mathcal{A}$ . In Figure 21 we plot the  $\tilde{\mathcal{I}}^{\text{KM}}$  images for the square on the top row, and the disc on the bottom row, for array lengths  $l_{\text{arr}} = 160, 140, 120$  m from left to right respectively. We observe that the quality of the image deteriorates for smaller arrays, and specifically the images for the disc exhibit narrower focusing to the the left endpoint of its horizontal diameter.

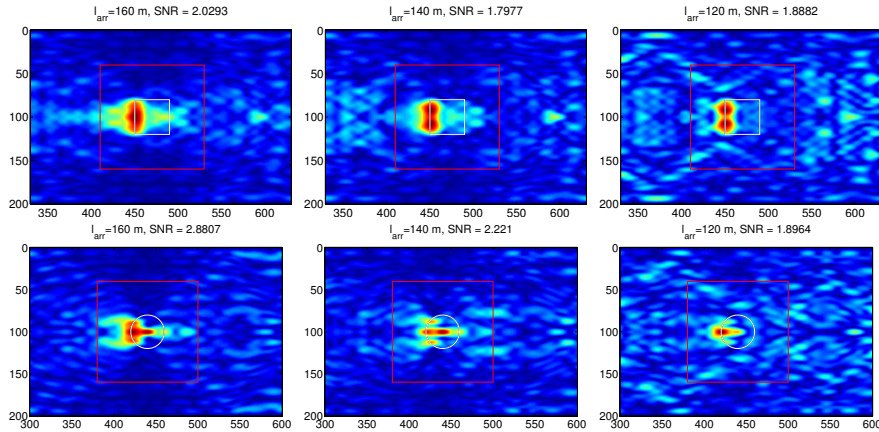


Figure 21: Imaging with  $\tilde{\mathcal{I}}^{\text{KM}}$  for the square (top) and the disc (bottom), when  $l_{\text{arr}} = 160, 140, 120$  m, for  $f = 73$  Hz and  $\varepsilon^+ = 0.02$ .

We continue decreasing the length of the array until it covers the half of the waveguide depth, i.e.  $l_{\text{arr}} = 100$  m. The leftmost subplot in Figure 22 depicts the  $\tilde{\mathcal{I}}^{\text{KM}}$  image for the square scatterer. This is a more ‘noisy’ image compared to those on the top row of Figure 21, and the SNR has dropped. In order to improve the quality of the image, we experiment with  $\tilde{\mathcal{I}}^{\text{KM},f}$  (see (9)). The middle subplot in Figure 22 is

derived by projecting on the first and second singular vectors of  $\widehat{\mathbb{P}}$ , while for the one on the right we project on the first and third singular vectors. The middle image exhibits less noise and increased SNR, and it is focused mainly towards the endpoints of the of the illuminated side, while the right image mainly focuses on its midpoint.

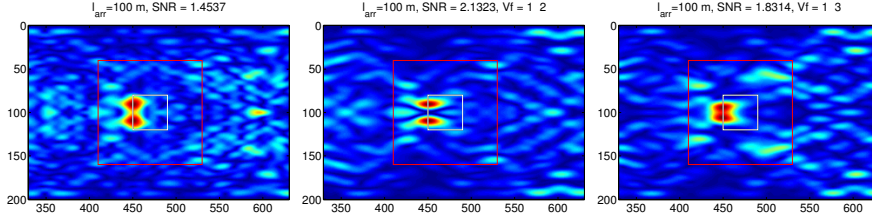


Figure 22: Imaging with  $\widetilde{\mathcal{I}}^{\text{KM}}$  (left) and  $\widetilde{\mathcal{I}}^{\text{KM},f}$  when projecting on singular vectors 1, 2 (middle) and 1, 3 (right), when  $l_{\text{arr}} = 100$  m, for  $f = 73$  Hz and  $\varepsilon^+ = 0.02$ .

It seems that the limiting case, at least for the current setup, is to consider an array with length equal to  $l_{\text{arr}} = 80$  m. In the leftmost subplot of Figure 23 we display the  $\widetilde{\mathcal{I}}^{\text{KM}}$  image, which, although being quite ‘noisy’, seems to locate the square-shaped scatterer. We then examine whether  $\widetilde{\mathcal{I}}^{\text{KM},f}$  may improve the quality of the image. Indeed, when we project on the first three singular vectors of  $\widehat{\mathbb{P}}$  we obtain the middle image in Figure 23, while the outcome of projecting on the first two singular vectors is the image on the right. Both of them are slightly improved compared to the  $\widetilde{\mathcal{I}}^{\text{KM}}$  image.

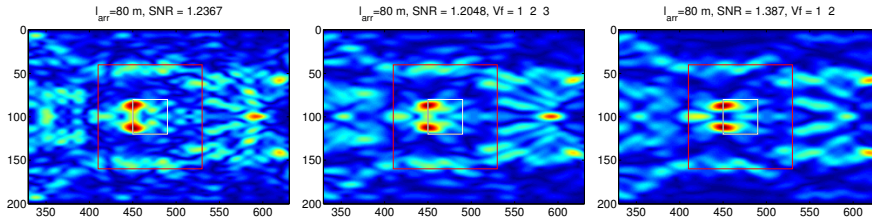


Figure 23: Imaging with  $\widetilde{\mathcal{I}}^{\text{KM}}$  (left) and  $\widetilde{\mathcal{I}}^{\text{KM},f}$  when projecting on singular vectors 1, 2, 3 (middle), and 1, 2 (right), for  $l_{\text{arr}} = 80$  m,  $f = 73$  Hz and  $\varepsilon^+ = 0.02$ .

## 5.2. Depth-dependent sound speed

As a step towards a more realistic marine environment we assume that the speed of sound in the water is a function of depth. Then we no longer have an analytic expression for the eigenvalues and the vertical eigenfunctions  $X_n$ , and we compute them numerically solving the associated Sturm-Liouville eigenvalue problem. However, the  $X_n$ ’s still form an orthonormal basis of  $L^2[0, D]$ , hence everything we did up to here carries over to this case too. The sound speed profile that we consider in our experiments is shown in Figure 24, and is adapted from [14] to fit the current waveguide setup.

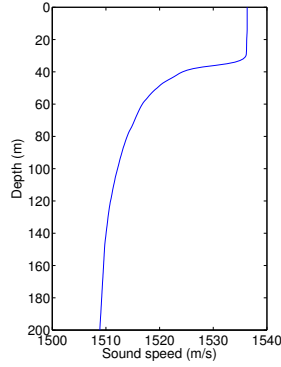


Figure 24: Depth-dependent sound speed profile for our waveguide.

On the top of Figure 25 we plot the  $\tilde{\mathcal{I}}^{\text{KM}}$  image for an array with length  $l_{\text{arr}} = 180$  m. In the bottom row, we show selective imaging results with  $\tilde{\mathcal{I}}_J^{\text{KM}}$ . All images are very similar to the corresponding ones for the homogeneous case shown in Figures 19 and 20, with its SNR values being slightly increased.

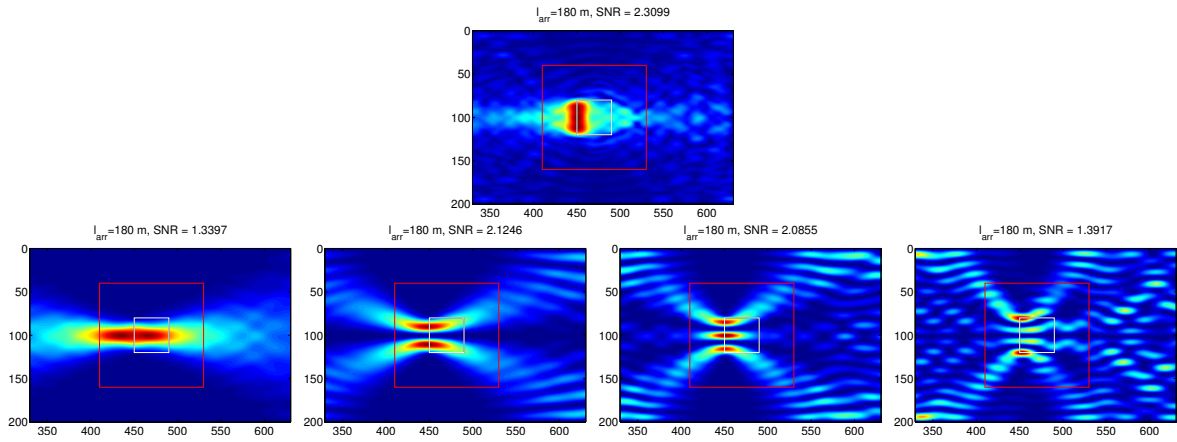


Figure 25: Top: Imaging with  $\tilde{\mathcal{I}}^{\text{KM}}$  for the square. Bottom: Selective imaging with  $\tilde{\mathcal{I}}_J^{\text{KM}}$ , for  $J = 1, 2, 3, 4$ . ( $l_{\text{arr}} = 180$  m,  $f = 73$  Hz.)

For smaller arrays, as in the case of a homogeneous medium, we have to impose a threshold  $\varepsilon^+$  to compute  $\tilde{S}$ . Here we adopt  $\varepsilon^+ = 0.022$ , which again implies that we project  $\hat{\Pi}$  just on the trigonometric polynomials that are supported mainly on  $\mathcal{A}$ . In Figure 26 we plot the  $\tilde{\mathcal{I}}^{\text{KM}}$  images for the square-shaped scatterer, for array lengths  $l_{\text{arr}} = 160, 140, 120$  m from left to right, respectively. All images illuminate the left side of the scatterer; compare with the corresponding images for constant sound speed, shown on the top row of Figure 21.

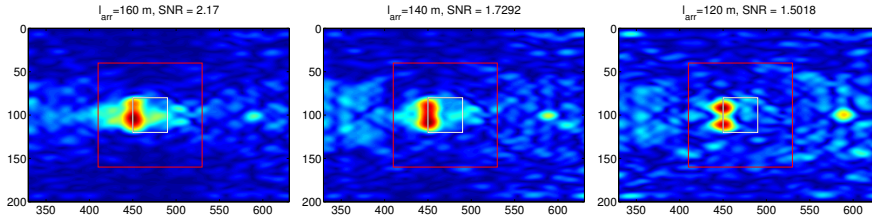


Figure 26: Imaging with  $\tilde{\mathcal{I}}^{\text{KM}}$  for the square, for  $l_{\text{arr}} = 160, 140, 120$  m, respectively,  $f = 73$  Hz and  $\varepsilon^+ = 0.022$ .

Images shown in Figure 27 are extracted with an array length equal to  $l_{\text{arr}} = 100$  m. The  $\tilde{\mathcal{I}}^{\text{KM}}$  image on the left hand side, may be further improved using  $\tilde{\mathcal{I}}^{\text{KM},f}$ . The middle subplot depicts the  $\tilde{\mathcal{I}}^{\text{KM},f}$  image that we obtain when we project on the first two singular vectors of  $\hat{\mathbb{P}}$ , and the right one when we project on the singular vectors 1 and 3. Both of them are improved compared to the  $\tilde{\mathcal{I}}^{\text{KM}}$  image exhibiting much higher SNR.

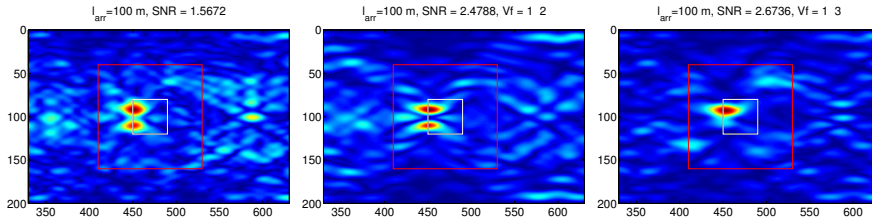


Figure 27: Imaging with  $\tilde{\mathcal{I}}^{\text{KM}}$  (left) and  $\tilde{\mathcal{I}}^{\text{KM},f}$  when projecting on singular vectors 1, 2 (middle) and 1, 3 (right), for  $l_{\text{arr}} = 100$  m,  $f = 73$  Hz and  $\varepsilon^+ = 0.022$ .

Finally, we decrease the array length to  $l_{\text{arr}} = 80$  m. Likewise the homogeneous case, the  $\tilde{\mathcal{I}}^{\text{KM}}$  image shown on the left subplot of Figure 28 is quite noisy but it seems to locate the object. Using  $\tilde{\mathcal{I}}^{\text{KM},f}$  and projecting on the first three and first two singular vectors of  $\hat{\mathbb{P}}$  leads to improved images as shown in the middle and right subplots of Figure 28, respectively.

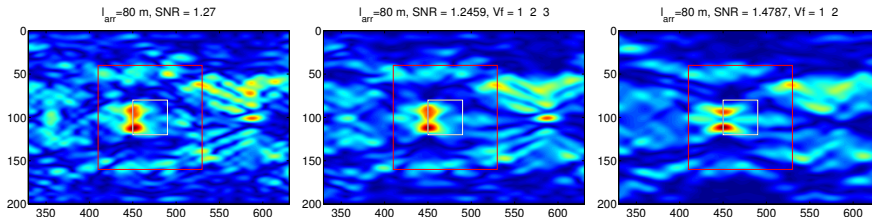


Figure 28: Imaging with  $\tilde{\mathcal{I}}^{\text{KM}}$  (left) and  $\tilde{\mathcal{I}}^{\text{KM},f}$  when projecting on singular vectors 1, 2, 3 (middle), and 1, 2 (right), for  $l_{\text{arr}} = 80$  m,  $f = 73$  Hz and  $\varepsilon^+ = 0.022$ .

The corresponding images for the disc-shaped scatterer for the depth-dependent sound speed profile are analogous to those for the square, therefore we do not show them here for sake of brevity.

## 6. Conclusions

In this work we considered the problem of locating and imaging extended reflectors in a waveguide using an active array of sensors. To image we use an imaging functional introduced in [36],  $\tilde{\mathcal{I}}^{\text{KM}}$ , that is a variation of Kirchhoff migration where instead of back propagating the array response matrix  $\hat{\Pi}$ , we back propagate a weighted modal projection of this, denoted  $\hat{\mathbb{P}}$ . For an array that spans the whole waveguide depth, the definition of  $\hat{\mathbb{P}}$  is straightforward and consists in integrating over the array  $\hat{\Pi}$  against the modes, *i.e.*, the eigenfunctions of the corresponding two-point vertical eigenvalue problem in the waveguide. To analyse the properties of  $\tilde{\mathcal{I}}^{\text{KM}}$  we have considered a simplified model problem where the scatterer is a vertical ‘screen’. By investigating this problem we showed that there is a relation between the singular vectors of  $\hat{\mathbb{P}}$  and the prolate spheroidal wave functions. More precisely, we observed that when the screen is fixed on the surface of the waveguide, we recover exactly the prolate spheroidal wave functions. Although this is not the case for other positions of the screen, selective imaging with  $\tilde{\mathcal{I}}^{\text{KM}}$  still exhibits a prolate-like behavior, in the sense that projection on the singular vectors that correspond to the largest singular values results in an image that focuses on the bulk of the screen, projection on singular vectors that correspond to intermediate singular values results in an image that focuses on the endpoints of the screen, while projection on singular vectors that correspond to very small in magnitude singular values does not provide any information about the position and the size of the screen.

The main contribution of this paper is that we have considered the case of arrays with partial aperture that do not span the whole depth of the waveguide. In that case, the main difficulty lies on the definition of the weighted modal projection  $\hat{\mathbb{P}}$  which should be adequately modified in order to preserve the nice properties we observed in the full array case. Remark that in this case the modes are no longer orthonormal on the array and we use instead the corresponding prolate (or prolate like) spheroidal wave functions on the array to define  $\hat{\mathbb{P}}$ . As the array aperture decreases we propose to use only the prolate functions whose support lies inside the array aperture and this introduces a natural regularization to the imaging problem.

We have seen that for the screen model problem, imaging with  $\tilde{\mathcal{I}}^{\text{KM}}$ , even if we remove half of the length of the originally full array, still creates images that are identical to those created with a full array-aperture! Furthermore,  $\tilde{\mathcal{I}}^{\text{KM}}$  is able to locate the screen with an array that has length equal to 10% of the waveguide’s depth.

We have also examined the performance of the proposed imaging functionals in the presence of additive noise, in the case of extended reflectors such as a square and a disc, as well as, for a non-homogeneous waveguide with a depth dependent velocity profile. In all these cases, our numerical results suggest that we can successfully image the scatterers even when we remove half of the array in length.

## Acknowledgements

This work was performed in the framework of the PEFYKA project within the KRIPIS section of the GSRT. The project is funded by Greece and the European Regional Development Fund of the European Union under the NSRF and the O.P. Competitiveness and Entrepreneurship. This work was also partially supported by the ERC Starting Grant Project ADAPTIVES-239959.

## References

- [1] A. L. Andrew. Eigenvectors of certain matrices. *Linear Algebra and Appl.*, 7:151–162, 1973.
- [2] T. Arens, D. Gintides, and A. Lechleiter. Direct and inverse medium scattering in a three-dimensional homogeneous planar waveguide. *SIAM Journal on Applied Mathematics*, 71(3):753–772, 2011.
- [3] J.-P. Berenger. A perfectly matched layer for the absorption of electromagnetic waves. *Journal of Computational Physics*, 114:185 – 200, 1994.
- [4] N. Bleistein. *Mathematical methods for wave phenomena*. Computer Science and Applied Mathematics. Academic Press Inc., Orlando, FL, 1984.
- [5] N. Bleistein, J. K. Cohen, and J. W. Stockwell, Jr. *Mathematics of multidimensional seismic imaging, migration, and inversion*, volume 13 of *Interdisciplinary Applied Mathematics*. Springer-Verlag, New York, 2001. Geophysics and Planetary Sciences.
- [6] L. Borcea, G. Papanicolaou, and F. Guevara Vasquez. Edge illumination and imaging of extended reflectors. *SIAM J. Imaging Sci.*, 1:75–114, 2008.
- [7] L. Borcea, G. Papanicolaou, and C. Tsogka. Optimal waveform design for array imaging. *Inverse Problems*, 23(5):1973–2020, 2007.
- [8] L. Bourgeois and E. Lunéville. The linear sampling method in a waveguide: a modal formulation. *Inverse problems*, 24(1):015018, 2008.
- [9] L. Bourgeois and E. Lunéville. On the use of sampling methods to identify cracks in acoustic waveguides. *Inverse Problems*, 28(10):105011, 2012.
- [10] J. L Buchanan, R. P Gilbert, A. Wirgin, and Y. Xu. *Marine acoustics: direct and inverse problems*. Siam, 2004.
- [11] S. Dediu and J. R. McLaughlin. Recovering inhomogeneities in a waveguide using eigensystem decomposition. *Inverse Problems*, 22(4):1227–1246, 2006.
- [12] S.D. Gedney. An anisotropic perfectly matched layer-absorbing medium for the truncation of FDTD lattices. *IEEE Transactions on Antennas and Propagation*, 44:1630 –1639, 1996.
- [13] U. Grenander and G. Szegő. *Toeplitz forms and their applications*. Chelsea Publishing Co., New York, second edition, 1984.
- [14] J.-P. Hermand and P. Gerstoft. Inversion of broad-band multitone acoustic data from the yellow shark summer experiments. *IEEE J. Ocean. Eng.*, 21:324–346, 1996.
- [15] W.S. Hodgkiss, H.C. Song, W.A. Kuperman, T. Akal, C. Ferla, and D.R. Jackson. A long-range and variable focus phase-conjugation experiment in shallow water. *The Journal of the Acoustical Society of America*, 105(3):1597–1604, 1999.
- [16] M. Ikehata, G. N. Makrakis, and G. Nakamura. Inverse boundary value problem for ocean acoustics using point sources. *Mathematical Methods in the Applied Sciences*, 27(12):1367–1384, 2004.
- [17] F.B. Jensen, W.A. Kuperman, M.B. Porter, and H. Schmidt. *Computational Ocean Acoustics*. Modern Acoustics and Signal Processing. Springer, 2011.
- [18] W.A. Kuperman and D. Jackson. Ocean acoustics, matched-field processing and phase conjugation. *Topics in Applied Physics*, pages 43–97. Springer Berlin / Heidelberg, 2002.
- [19] H. J. Landau and H. O. Pollak. Prolate spheroidal wave functions, fourier analysis and uncertainty – II. *Bell System Technical Journal*, 40(1):65–84, 1961.

- [20] H. J. Landau and H. O. Pollak. Prolate spheroidal wave functions, fourier analysis and uncertainty – III: The dimension of the space of essentially time- and band-limited signals. *Bell System Technical Journal*, 41(4):1295–1336, 1962.
- [21] P. Monk and V. Selgas. Sampling type methods for an inverse waveguide problem. *Inverse Problems and Imaging*, 6(4):709–747, 2012.
- [22] Montjoie user’s guide, <http://montjoie.gforge.inria.fr/>.
- [23] I. C. Moore and M. Cada. Prolate spheroidal wave functions, an introduction to the Slepian series and its properties. *Appl. Comput. Harmon. Anal.*, 16(3):208–230, 2004.
- [24] N. Mordant, C. Prada, and M. Fink. Highly resolved detection in a waveguide using the D.O.R.T. method. *J. Acoust. Soc. Amer.*, 105:2634–2642, 1999.
- [25] J. A. Morrison. On the eigenfunctions corresponding to the bandpass kernel, in the case of degeneracy. *Quart. Appl. Math.*, 21:13–19, 1963.
- [26] B. Pinçon and K. Ramdani. Selective focusing on small scatterers in acoustic waveguides using time reversal mirrors. *Inverse Problems*, 23:1–25, 2007.
- [27] C. Prada, J. de Rosny, D. Clorennec, J.-G. Minonzio, A. Aubry, M. Fink, L. Berniere, P. Billand, S. Hibrat, and T. Folegot. Experimental detection and focusing in shallow water by decomposition of the time reversal operator. *J. Acoust. Soc. Amer.*, 122:761–768, 2007.
- [28] M. Rosenblatt. Some purely deterministic processes. *J. Math. Mech.*, 6:801–810, 1957.
- [29] I. SenGupta, B. Sun, W. Jiang, G. Chen, and M. C. Mariani. Concentration problems for bandpass filters in communication theory over disjoint frequency intervals and numerical solutions. *J. Fourier Anal. Appl.*, 18(1):182–210, 2012.
- [30] S. Serra. On the extreme eigenvalues of hermitian (block) toeplitz matrices. *Linear Algebra and its Applications*, 270(1–3):109 – 129, 1998.
- [31] D. Slepian. Prolate spheroidal wave functions, fourier analysis and uncertainty – IV: Extensions to many dimensions; generalized prolate spheroidal functions. *Bell System Technical Journal*, 43(6):3009–3057, 1964.
- [32] D. Slepian. Prolate spheroidal wave functions, fourier analysis, and uncertainty – V: The discrete case. *Bell System Technical Journal*, 57(5):1371–1430, 1978.
- [33] D. Slepian. Some comments on Fourier analysis, uncertainty and modeling. *SIAM Rev.*, 25(3):379–393, 1983.
- [34] D. Slepian and H. O. Pollak. Prolate spheroidal wave functions, Fourier analysis and uncertainty – I. *Bell System Tech. J.*, 40:43–63, 1961.
- [35] W. F. Trench. Asymptotic distribution of the even and odd spectra of real symmetric Toeplitz matrices. *Linear Algebra Appl.*, 302/303:155–162, 1999. Special issue dedicated to Hans Schneider (Madison, WI, 1998).
- [36] C. Tsogka, D. A. Mitsoudis, and S. Papadimitropoulos. Selective imaging of extended reflectors in two-dimensional waveguides. *SIAM J. Imaging Sci.*, 6(4):2714–2739, 2013.